An uncertainty principle for neural coding: Conjugate representations of position and velocity are mapped onto firing rates and co-firing rates of neural spike trains

Ryan Grgurich and Hugh T. Blair

Psychology Department, UCLA, Los Angeles, CA;

Abstract. The hippocampal system contains neural populations that encode an animal's position and velocity as it navigates through space. Here, we show that a population of spiking neurons can map information about position and velocity onto two orthogonal codes—a *firing rate code* (R) and a *co-firing rate code* ($\dot{R}$)—which behave as *conjugates* of one another: if one code conveys information about position, then the other conveys information about velocity. We describe two biologically inspired methods for decoding R and $\dot{R}$, referred to as *sigma* and *sigma-chi* decoding, respectively. Simulations of head direction (HD) and grid cell spike trains show that if neural firing rates are tuned for position (but not velocity), then position is recovered from R via sigma decoding, whereas velocity is recovered from $\dot{R}$ via sigma-chi decoding. Conversely, simulations of an oscillatory interference code implemented by theta cell spike trains show that if co-firing rates are tuned for position (but not velocity), then position is recovered from $\dot{R}$ via sigma-chi decoding, whereas velocity is recovered from R via sigma decoding. This conjugate relationship between R and $\dot{R}$ mirrors the "uncertainty principle" from physics, in that the more information one code conveys about position, the more the other conveys about velocity, and vice versa. Theoretical models of hippocampal networks are often simulated using linear units that derive their outputs only from R, and not from $\dot{R}$. The conjugate coding principle implies that these models may be limited in their ability generate accurate predictions about connectivity within biological networks composed from nonlinear neurons that are capable of deriving their outputs from both R and $\dot{R}$.

INTRODUCTION

The rodent hippocampal system contains populations of neurons that encode an animal's position and velocity as it navigates through space. In the literature, these populations are named for variables that modulate their firing rates: "head-direction" (HD) cell firing rates are tuned for the angular position of the head (Taube et al., 1990), "grid" cell firing rates are periodically tuned for the animal's spatial position (Hafting et al., 2005), "place" cell firing rates are non-periodically tuned for the animal's spatial position (O'Keefe & Dostrovsky, 1971), "border" (or "boundary") cell firing rates increase (or decrease) near environmental boundaries (Solstad et al., 2008; Savelli et al., 2008; Lever et al., 2009), "speed" cell firing rates increase (or decrease) in proportion with the animal's running speed (Kropf et al., 2015; Hinman et al., 2016; Gois & Tort, 2018), and "theta" cell firing rates are temporally modulated by 4-12 Hz theta oscillations. Although these monikers accurately describe how the firing rates of individual neurons are tuned, they may not fully describe the information that such neurons encode at the population level, because populations of spiking neurons encode information not only in their firing rates, but in other ways as well.

In rodents, position-tuned neurons (such as place and grid cells) exhibit rhythmic modulation of their spike trains by theta rhythm. Information about the animal's position can be decoded not only from the firing rates of these neurons (Wilson and McNaughton, 1993), but also from the phases at which spikes occur relative to theta rhythm in the local field potential (O'Keefe and Recce, 1993; Skaggs et al., 1996; Jensen and Lisman, 2000; Hafting et al., 2008; Climer et

al., 2013; Jeewajee et al., 2013). Hence, spatially tuned neurons can encode the animal's position in two ways: in their firing rates and firing phases. These two codes map the animal's position into different representational spaces. The firing rate code maps position into a space of "population vectors" where each dimension measures time intervals between pairs of spikes that are both fired by the *same* neuron (because a neuron's firing rate is simply the inverse of its mean interspike interval). By contrast, the phase code maps position into a space where each dimension measures time intervals (normalized by the theta cycle period) between pairs of spikes that are fired by *different* neurons. Hence, the phase code belongs to a general category of "cross-correlation" codes which map information onto intervals between pairs of spikes fired by different neurons ("between-cell" spike intervals), whereas the firing rate code is an "autocorrelation" code which maps information onto intervals between pairs of spikes fired by the same neuron ("within-cell" spike intervals). If neural populations can simultaneously encode information in their firing rates as well as their spike correlations, then how is information about the world distributed between these two different coding channels?

Here, we show that a neural population can simultaneously embed two orthogonal codes within its spike trains: a *firing rate code* derived from the spike trains of individual neurons, and a *co-firing rate code* derived from correlations between spike trains of different neurons. It is shown that these two codes behave as *conjugates* of one another: if firing rates convey information about position, then spike correlations convey information about velocity, and vice versa. This trade-off mirrors the uncertainty principle from physics, which states that the more we know about a particle's position, the less we know about its momentum (or velocity), and vice versa. An analogous uncertainty principle arises in neural coding of position and velocity: the more accurately a neural population encodes position information in its firing rates (or co-firing rates), the less accurately velocity information can be encoded in those same firing rates (or co-firing rates). However, because of the conjugate relationship between firing rates and co-firing rates, mapping position information onto firing rates allows velocity information to be concurrently mapped onto co-firing rates, and vice versa. Consequently, a single neural population can simultaneously encode orthogonal representations of both position and velocity in its spike trains.

Theoretical models of hippocampal networks have been proposed to explain how neural populations that encode position and velocity—such as place cells, grid cells, border cells HD cells, speed cells, and theta cells—might be functionally interconnected with one another to solve navigational problems such as cognitive mapping, self-localization, and trajectory planning (for review see Hinman et al., 2018). Many of these models are composed from simplified linear neurons that derive their outputs by computing weighted sums of their firing rate inputs, but such linear model neurons cannot effectively extract information from spike train correlations (a circuit of linear neurons would be required for this). By contrast, biological neurons exhibit complex branching patterns and electrotonic structure that allow them to derive their outputs via nonlinear integration of their inputs (for review see Mel, 2007). The conjugate coding principle described here implies that biological neurons in hippocampal networks may be capable of extracting information about position and velocity from their inputs in ways that would not be possible within artificial networks composed from linear integrator neurons. Hence, as argued in the Discussion, network models composed from linear neurons may not be well suited for generating accurate predictions about functional connections among neural populations that encode positon and velocity in the hippocampal system.

RESULTS

A single neuron's spike train shall be represented here by a neural response function stored as a series of binary values sampled synchronously at discrete time points,

$$\mathbf{s}_n = \{s_n[t_0], s_n[t_1], \cdots, s_n[t_k], \cdots, s_n[t_K]\}, \quad \text{(Eq.1)}$$

where $s_n[t_k] = 1$ if neuron n fires a spike at time t_k, and $s_n[t_k] = 0$ otherwise. A fixed sampling rate of 1 KHz shall be used for all simulations. Spike trains generated by a population of N neurons are stored in a spike response matrix:

$$\mathbf{S} = \begin{bmatrix} \mathbf{s}_1 \\ \mathbf{s}_2 \\ \vdots \\ \mathbf{s}_N \end{bmatrix} = \{S_0, S_1, \ldots, S_k, \ldots, S_K\}, \quad \text{(Eq. 2)}$$

where each row, $\mathbf{s}_n$, contains the neural response function of a different neuron, and each column, $S_k = \{s_1[t_k], s_2[t_k], \ldots, s_N[t_k]\}^T$, contains a population vector of binary values flagging which neurons fired a spike at time t_k.

Computing angular velocity by differentiating HD cell spike trains

In this section, spike trains of HD cells are simulated to encode an animal's angular head position—but not angular head velocity—in their firing rates. It is shown that head angle can be recovered from the HD cell population's firing rates by process referred to as *sigma decoding*. It is further shown that even if individual neurons do not encode information about angular velocity in their firing rates, velocity information can nonetheless be recovered from the HD cell population's co-firing rates by a process referred to as *sigma-chi decoding*. Hence, the sigma-chi decoder can be regarded as a neural differentiator that derives a velocity signal from a position signal.

Simulation of HD cell spike trains

Simulated HD cell spike trains were generated from head angle data obtained while a behaving rat foraged freely for food pellets in a cylindrical arena (see Methods). Tracking data was upsampled to 1 KHz to match the spike train simulation rate, yielding a time series of head azimuth angles, $\mathbf{q} = \{q_0, q_1, \cdots, q_k, \cdots, q_K\}$. HD cell tuning curves were simulated by a Von Mises distribution, so that the probability of HD cell n firing a spike at time t_k was given by:

$$p_n[t_k] = R_{max} \frac{e^{\kappa \cos(q_k - \hat{q}_n)}}{2\pi I_0(\kappa)} dt, \quad \text{(Eq. 3)}$$

where $\hat{q}_n$ is the preferred firing direction for neuron n, R_{max} is the peak firing rate of the HD cell in Hz, κ is a concentration parameter which regulates the HD tuning width, $I_0(\kappa)$ is the modified Bessel function of order 0, and dt=1 ms is the time bin resolution. Note that parameters R_{max} and κ are not indexed by n, because all HD cells shared the same values of these parameters. Fig. 1A shows HD tuning curves for $N = 12$ simulated HD cells with $R_{max} = 100$ Hz and $\kappa = 0.5$. At each time step, the value of $p_n[t_k]$ was used as a binary threshold on the output of pseudorandom number generator, to stochastically determine whether HD cell n fired a spike at time t_k. The binary values generated by this stochastic process filled a spike response matrix (Eq. 2) for the HD cell population. Fig. 1B shows spike rasters for 12 simulated HD cells during a 10 s segment of head angle data.

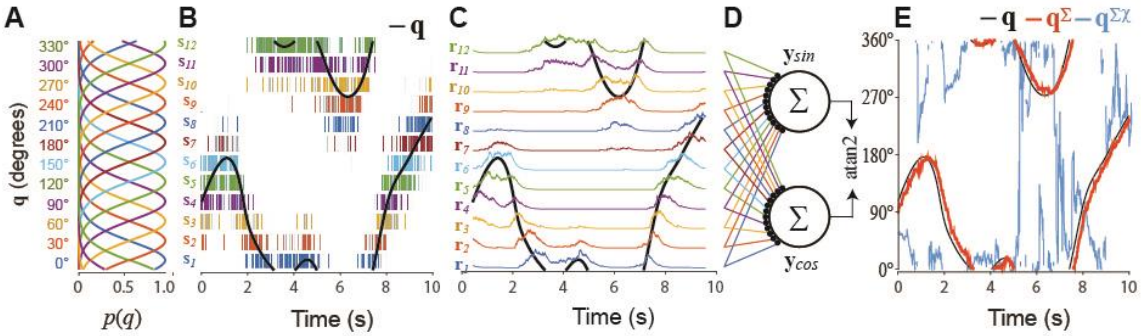

Figure 1. *Sigma decoder recovers head angle from HD cell firing rates.* A) Von Mises tuning functions were used to simulated spike trains of 12 HD cells. B) Black line shows 10 s sample of head angle data, $\mathbf{q}$; rasters show spike trains of 12 HD cells. C) Head angle data (black line) superimposed over colored lines showing HD cell firing rates derived by Eq. 5 (τ_u=200 ms). D) Sigma neurons sum HD cell firing rates to decode sine and cosine components of the head angle. E) Arctangent function recovers the estimated head angle, $\mathbf{q}^{\Sigma}$, from its sine and cosine components; head angle cannot be recovered by the sigma-chi deocder, $\mathbf{q}^{\Sigma\chi}$.

Sigma decoding: Recovering head angle from HD cell firing rates

The head angle can be recovered from simulated HD cell spike trains using a standard vector summation method for decoding neural firing rates. This method—henceforth referred to as *sigma decoding*—involves three steps, which can be written as a sequence of mapping functions: $\mathbf{S} \rightarrow \mathbf{R} \rightarrow \mathbf{Y} \rightarrow \mathbf{q}^{\Sigma}$. The first step, $\mathbf{S} \rightarrow \mathbf{R}$, converts spike trains into firing rates via a process that mimics temporal integration of spike trains at synapses. The second step, $\mathbf{R} \rightarrow \mathbf{Y}$, computes weighted sums of firing rates to obtain estimates for the sine and cosine components of the head angle. The third step, $\mathbf{Y} \rightarrow \mathbf{q}^{\Sigma}$, applies the arctangent function to estimate the head angle from its sine and cosine components. We shall write $\mathbf{q}^{\Sigma}$ to denote the time series of estimated head angles generated by the sigma decoder.

<u>Step 1: Converting spike trains into firing rates</u>. HD cell spike trains were converted into firing rates via a process intended to mimic temporal integration at synapses. The input to this process is a spike response matrix $\mathbf{S}$ (Eq. 2)**,** and the output is a *firing rate response matrix*:

$$\mathbf{R} = \begin{bmatrix} \mathbf{r}_1 \\ \mathbf{r}_2 \\ \vdots \\ \mathbf{r}_N \end{bmatrix} = \{R_0, R_1, \dots, R_k, \dots, R_K\}. \qquad \text{(Eq. 4)}$$

Each column of this matrix, $R_k = \{r_1[t_k], r_2[t_k], \dots, r_N[t_k]\}^T$, is a population vector containing instantaneous HD cell firing rates measured at time t_k. Each row, $\mathbf{r}_n = \{r_n[t_0], r_n[t_1], \cdots, r_n[t_K]\}$, is a time series of firing rate estimates for a single HD cell obtained by convolving its spike train with an exponential decay kernel,

$$\mathbf{r}_n = \mathbf{s}_n * \mathbf{u}. \qquad \text{(Eq. 5)}$$

Individual elements of the decay kernel, $\mathbf{u} = \{u_0, u_1, \dots, u_l, \dots, u_\infty\}$, are given by

$$u_l = e^{-l/\tau_u}, \qquad \text{(Eq. 6)}$$

where τ_u is the decay constant, and l indexes time bins with positive offsets from $p_n[t_k]$ (kernel weights were uniformly zero for negative time offsets). Fig. 1C illustrates examples of simulated HD cell firing rates with $\tau_u = 200$ ms.

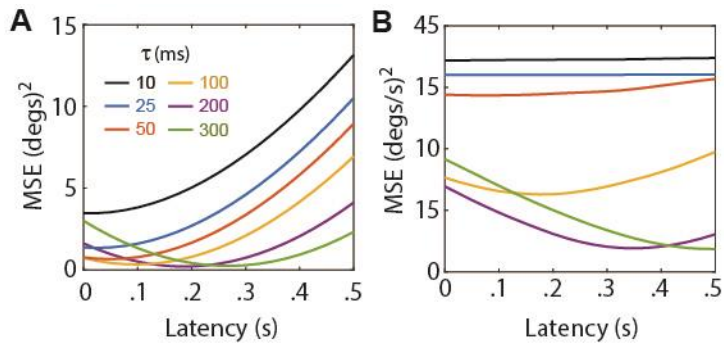

Figure 2. *Accuracy-latency tradeoff for spike train decoding.* A) Mean-squared error (MSE; y-axis) for decoding angular head position from HD cell firing rates at varying latencies (x-axis); larger decay constants (τ) improve decoding accuracy at a cost of increased latency. B) MSE for decoding angular velocity from HD cell co-firing rates at varying latencies; optimal latencies are apporximately doubled from those in 'A' because the sigma-chi decoder of co-firing rates uses two temporal integration steps.

<u>Step 2: Converting firing rates into angle components</u>. Firing rates were converted into sine and cosine components of the head angle via spatial integration of synaptic inputs to a pair of sigma units (Fig 1D) that decoded $\sin(\mathbf{q})$ and $\cos(\mathbf{q})$. Activation of these two sigma units can be represented by a response matrix, $\mathbf{Y} = \{\mathbf{y}_{sin}, \mathbf{y}_{cos}\}^T = \{Y_0, Y_1, \dots, Y_k, \dots, Y_K\}$, where the two rows $\mathbf{y}_{sin}$ and $\mathbf{y}_{cos}$ are time series of decoded estimates for $\sin(\mathbf{q})$ and $\cos(\mathbf{q})$, and each column $Y_k = \{sin_k, cos_k\}^T$ contains the estimated sine and cosine of the decoded head angle at time t_k. The output from decoder neuron m was computed as a weighted sum of its firing rate inputs:

$$y_m[t_k] = \sum_{n=1}^{N} w_{m,n} \mathrm{r}_m[t_k]$$

(Eq. 7)

where $w_{m,n}$ is a synaptic weight assigned to the nth spike train input received by decoder neuron m. The input weights were $w_{m,n} = \sin(2\pi n/N)$ or $w_{m,n} = \cos(2\pi n/N)$ for the sine versus cosine decoder neurons, respectively.

<u>Recovering head angle via the arctangent function</u>. The final decoding step, $\mathbf{Y} \rightarrow \mathbf{q}^{\Sigma}$, was performed by taking the arctangent of decoder neuron outputs at each time step:

$$q_k^{\Sigma} = \mathrm{atan2}(sin_k, cos_k). \qquad \text{(Eq. 8)}$$

Figure 1E shows that $\mathbf{q}^{\Sigma}$ (red line) provides an accurate estimate of $\mathbf{q}$ (black line), except that $\mathbf{q}^{\Sigma}$ is delayed in time with respect to $\mathbf{q}$ by a latency that is approximately equal to the exponential decay constant ($\tau_u = 200$ ms for the simulation shown). The dynamics of the animal's head turning set an upper bound on τ_u, because the decay constant must not be set so large that $\mathbf{q}$ can vary widely within the span of the integration time window. Below this upper bound, there is a tradeoff between accuracy and latency of the decoded position signal, such that increasing τ_u to integrate over longer time periods improves the accuracy of $\mathbf{q}^{\Sigma}$ (since a larger time window contains more spikes and thus more information), at a cost of delaying the decoded signal in time (Fig. 2A). This type of latency shift can be eliminated if inputs to the decoder are modulated by velocity as well as position (Eliasmith, 2005), but this trick will not be utilized here, because our purpose is to

demonstrate how velocity information can be recovered from co-firing rates in the case where individual firing rates exclusively encode position, and contain no information about velocity.

Sigma-chi decoding: Recovering angular velocity from HD cell co-firing rates

Simulated HD cell firing rates were modulated only by the angular head position, $\mathbf{q}$, and not by the angular head velocity $\dot{\mathbf{q}}$ (Eq. 3). Nonetheless, $\dot{\mathbf{q}}$ can be decoded from HD cell spike trains using a process we shall refer to as *sigma-chi decoding*, which involves a sequence of three steps: $\mathbf{S} \rightarrow \vec{\mathbf{X}} \rightarrow \dot{\mathbf{R}} \rightarrow \dot{\mathbf{q}}^{\Sigma\chi}$. The first step, $\mathbf{S} \rightarrow \vec{\mathbf{X}}$, performs nonlinear integration on pairs of spike trains to derive a quantity we call the *chi rate*. The second step, $\vec{\mathbf{X}} \rightarrow \dot{\mathbf{R}}$, pools chi rates to extract a vector of *co-firing rates* that form a frequency domain representation of angular velocity, encoded by a population of neurons called *sigma-chi units*. The third step, $\dot{\mathbf{R}} \rightarrow \dot{\mathbf{q}}^{\Sigma\chi}$, decodes angular head velocity from sigma-chi units via vector summation of co-firing rates. We write $\dot{\mathbf{q}}^{\Sigma\chi}$ to denote the time series of angular head velocities recovered by the sigma decoder.

<u>Step 1: Deriving chi rates from spike train pairs</u>. The firing rate of a single spike train is inversely proportional to the interspike intervals (ISIs) between pairs of spikes in the train, and can thus be measured via leaky integration of the spike train (Eq. 5). We analogously define the *chi rate* for a pair of spike trains, i and j, to be a quantity that is inversely proportional to ISIs between pairs of spikes where one spike comes from neuron i, and the other from neuron j:

$$\boldsymbol{\chi}_{i,j} = \left(\mathbf{s}_i \circ \mathbf{r}_j\right) * \mathbf{v}, \qquad \text{(Eq. 9)}$$

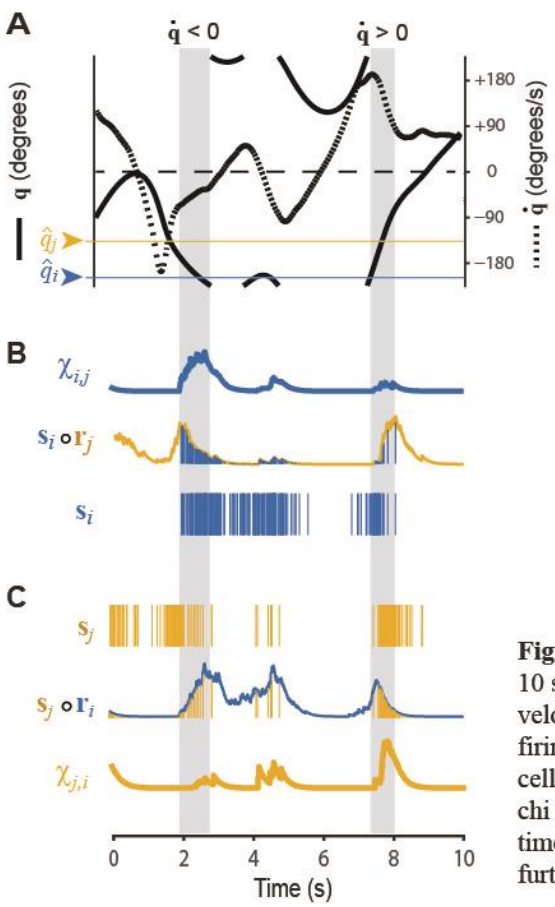

Figure 3. *Chi rates for a pair of HD cells.* A) Solid line shows 10 s sample of the head angle $\mathbf{q}$, dashed line shows angular head velocity $\dot{\mathbf{q}}$ during the same period; colored lines show preferred firing directions for HD cells *i* and *j* (which are the same as HD cells 1 and 3, respeectively, from Fig. 1). B,C) Dependency of chi rates $\chi_{i,j}$ (B) and $\chi_{j,i}$ (C) upon angular velocity during two time periods when $\dot{\mathbf{q}}$<0 and $\dot{\mathbf{q}}$>0 (gray shading; see main text for further explanation).

where $\boldsymbol{\chi}_{i,j}$ denotes the chi rate between spike trains i and j, $\circ$ denotes the element-wise product of same-length vectors, and $\mathbf{v}$ is an exponential decay kernel (exactly as in Eq. 5, but with a different decay constant, τ_v). The term $\mathbf{s}_i \circ \mathbf{r}_j$ may be regarded as a "carbon copy" of $\mathbf{s}_i$ in which spikes no longer have unit amplitude, but instead have a real-valued amplitude that is scaled by $\mathbf{r}_j$. After the spike amplitudes are scaled, they are temporally integrated by the exponential decay kernel, $\mathbf{v}$. Hence, the chi rate is derived by sequential integration with two decay constants: τ_u (Eq. 5) and τ_v (Eq. 9). For simplicity, we set $\tau_u = \tau_v$ for all simulations presented here. However, setting these decay constants to different values may sometimes help to improve the accuracy of decoding information from co-firing rates. Possible biological substrates for computing the chi rate shall be considered in the Discussion.

Figure 3 illustrates how $\boldsymbol{\chi}_{i,j}$ is influenced by $\mathbf{q}$ and $\dot{\mathbf{q}}$ for the case where neurons i and j are HD cells with nearby preferred directions, $\hat{q}_i = 0°$ and $\hat{q}_j = 60°$. These two HD cells only generate spikes when the head angle is in the neighborhood of both $\hat{q}_i$ and $\hat{q}_j$, so clearly, $\boldsymbol{\chi}_{i,j}$ depends upon $\mathbf{q}$. However, $\boldsymbol{\chi}_{i,j}$ is also sensitive to $\dot{\mathbf{q}}$. To see why this is so, consider what happens during the two shaded periods in Figure 3, when the head angle passes through $\hat{q}_i$ and $\hat{q}_j$ in the clockwise ($\dot{\mathbf{q}} < 0$) versus counterclockwise ($\dot{\mathbf{q}} > 0$) directions. During the first period where $\dot{\mathbf{q}} < 0$, we see that $\boldsymbol{\chi}_{i,j}$ (Fig. 3B, blue) grows large, but $\boldsymbol{\chi}_{j,i}$ (Fig. 3C, yellow) does not. This is because neuron j spikes prior to neuron i, so that $\mathbf{r}_j$ is nonzero when $\mathbf{s}_i$ starts firing and $\mathbf{s}_i \circ \mathbf{r}_j$ grows large (Fig. 3B), but $\mathbf{r}_i$ is near zero when $\mathbf{s}_j$ starts firing so $\mathbf{s}_j \circ \mathbf{r}_i$ does not grow large (Fig. 3C). During the second shaded period where $\dot{\mathbf{q}} > 0$, exactly the opposite occurs, and therefore, $\boldsymbol{\chi}_{j,i}$ grows large but $\boldsymbol{\chi}_{i,j}$ does not. Hence, $\boldsymbol{\chi}_{i,j}$ for neighboring HD cells depends not only upon $\mathbf{q}$, but also upon $\dot{\mathbf{q}}$**.** To derive a signal that is dependent purely upon $\dot{\mathbf{q}}$ and not upon $\mathbf{q}$, we may pool $\boldsymbol{\chi}_{i,j}$ values across HD cell pairs that share the same angle of separation, $\Delta\hat{q}_{i,j}$.

<u>Step 2: Pooling chi rates to derive co-firing rates</u>. Given a population of N spiking neurons, there are N^2 unique ordered pairings between the neurons, including pairings of each neuron with itself (it is necessary to consider ordered rather than unordered pairings, since $\boldsymbol{\chi}_{i,j} \neq \boldsymbol{\chi}_{j,i}$). This forms an $N \times N$ matrix of chi rates. For HD cells, the rows and columns of this matrix can be sorted by preferred directions, $\hat{q}_1, \hat{q}_2 \cdots, \hat{q}_N$. If a time series of chi rates, $\boldsymbol{\chi}_{i,j}$, is placed in each matrix entry, then the combined entries form a time series of 2D matrices, henceforth denoted as $\vec{\mathbf{X}}$ (Fig. 4A). At each time slice t_k, $\vec{\mathbf{X}}$ contains a 2D matrix, $\mathbf{X}_k$, in which each entry is the instantaneous chi rate, $\chi_{i,j}[t_k]$, between a pair of HD cells, i and j. The main diagonal of $\mathbf{X}_k$ contains chi rates of HD cells paired with themselves; flanking the main diagonal there are $N - 1$ diagonal bands composed from entries containing chi rates between pairs of HD cells that share the same angle of separation, $\Delta\hat{q}_{i,j} = \hat{q}_j - \hat{q}_i$, between their preferred directions. These diagonal bands wrap around at the matrix edges, since $\Delta\hat{q}_{i,j}$ is a circular variable with periodic boundary conditions. We shall index these diagonal bands by $m = 0,1,2, \ldots, N-1$, such that the main diagonal ($i = j$) is indexed by $m = 0$, and each non-zero index m references a band containing chi rates between pairs of HD cells whose preferred directions are separated by a common angle, $\Delta\hat{q}_m = m \times 360°/N$. The activation of sigma-chi unit m can then be expressed as a co-firing rate, which is the sum of all chi rates along a single band (Fig. 4B):

$$\dot{r}_m[t_k] = \sum_{i=1}^{N} \chi_{i,\mathrm{mod}(i+m,N)}[t_k], \qquad \text{(Eq. 10)}$$

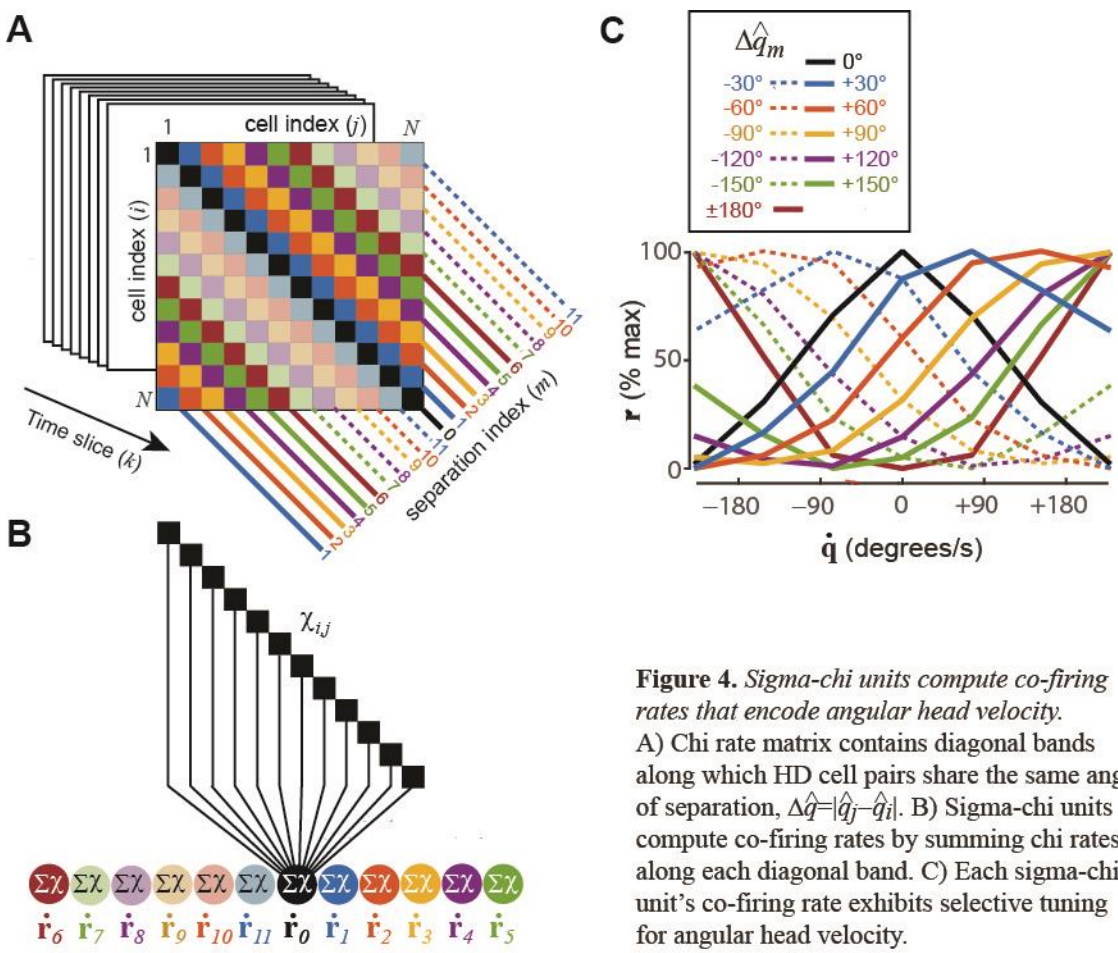

Figure 4. *Sigma-chi units compute co-firing rates that encode angular head velocity.* A) Chi rate matrix contains diagonal bands along which HD cell pairs share the same angle of separation, $\Delta\hat{q}=|\hat{q}_j-\hat{q}_i|$. B) Sigma-chi units compute co-firing rates by summing chi rates along each diagonal band. C) Each sigma-chi unit's co-firing rate exhibits selective tuning for angular head velocity.

where i indexes each of the matrix elements along diagonal m. By summing up chi rates in this way, sigma-chi units acquire direction-independent sensitivity to angular velocity.

The sensitivity of co-firing rates to angular velocity depends upon the time constants of temporal integration. τ_u and τ_v, and also upon the spatial separation, $\Delta\hat{q}_m$, between the preferred directions of HD cell pairs along the diagonal indexed by m. To see why this is so, it is helpful to think of $\dot{r}_m$ as a measurement of the change in head angle, Δq, over a specific time span, Δt. The duration of Δt is determined by τ_u and τ_v, so these decay constants should be chosen to maximize sensitivity within a representative range of angular velocities that occurs in the behavior data. In simulations presented here, we varied τ_u and τ_v to study their influence upon decoding accuracy (Fig. 2), but we did not permit different sigma-chi neurons to have different time constants (hence, in any given simulation, all of the sigma chi neurons integrated Δq across the same span of time). However, since each sigma-chi unit has its own value of $\Delta\hat{q}_m$, different units measure Δq with a different sized "yardstick." This endows each unit with its own preferred frequency of head rotation. The angular separations $\Delta\hat{q}_0, \Delta\hat{q}_1 \cdots, \Delta\hat{q}_{N-1}$ thus act like a set of spatial frequencies for representing angular velocity in the Fourier domain. This co-firing rate code for angular head velocity is conjugate and orthogonal to the firing rate code for angular head position. Sigma-chi units indexed by $m = 1,2,\ldots,(N/2)-1$ have positively sloped tuning functions (Fig. 4C, solid lines), and thus generate co-firing rates that are analogous to positive frequency components. Sigma-chi units indexed by $m = (N/2) + \{1,2,\ldots,(N/2)-1\}$ have negatively sloped tuning functions (Fig. 4C, dashed lines), and thus generate co-firing rates that are analogous to negative frequency

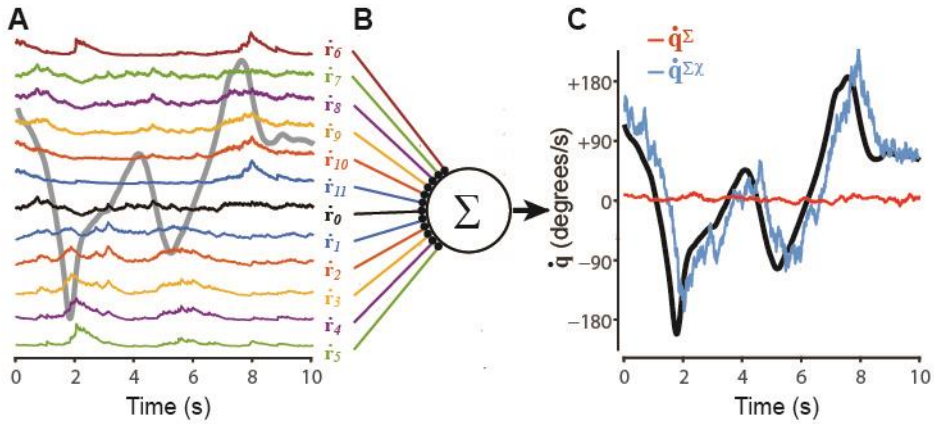

Figure 5. *Sigma-chi decoder recovers angular velocity from HD cell co-firing rates.* A) Colored lines show 10 s sample of co-firing rates computed by 12 sigma-chi units; gray line shows angular velocity during the simulation. B) True angular head velocity data (black) plotted alongside angular velocity signals recovered from co-firing rates via the sigma-chi decoder ($\dot{\mathbf{q}}^{\Sigma\chi}$), and from firing rates via the sigma decoder ($\dot{\mathbf{q}}^{\Sigma}$).

components. The unit indexed by $m = 0$ sums over the chi rates of each HD cell with itself, and symmetrically decreases its activity for turning in either direction. The unit indexed by $m = N/2$ (assuming even-valued N) sums over chi rates of HD cells that have 180° opposing preferred directions, and symmetrically increases its activity for turning in either direction. Activation of sigma-chi neurons is thus modulated by head turning in a manner that is quite similar to "angular velocity cells" that have been reported in the head direction system (Sharp, 1996; Stackman & Taube, 1998).

<u>Step 3: Decoding velocity from sigma-chi units</u>. Across time, the sigma-chi rates defined by Eq. 10 form a *co-firing rate response matrix*:

$$\dot{\mathbf{R}} = \begin{bmatrix} \dot{\mathbf{r}}_0 \\ \dot{\mathbf{r}}_1 \\ \vdots \\ \dot{\mathbf{r}}_{N-1} \end{bmatrix} = \{\dot{R}[t_0], \dot{R}[t_1], \dots, \dot{R}[t_{L-1}]\}. \qquad \text{(Eq. 11)}$$

Each row of this matrix, $\dot{\mathbf{r}}_m = \{\dot{r}_m[t_0], \dot{r}_m[t_1], \cdots, \dot{r}_m[t_K]\}$, stores a time series of co-firing rates generated by sigma-chi unit m (Fig. 5A). Each column, $\dot{R}[t_k] = \{\dot{r}_0[t_k], \dot{r}_1[t_k], \dots, \dot{r}_{N-1}[t_k]\}^T$, stores the instantaneous population vector of co-firing rates at time step k. A mapping from co-firing rates onto an estimate of the angular velocity, $\dot{\mathbf{R}} \rightarrow \dot{\mathbf{q}}^{\Sigma\chi}$, can be accomplished by computing a weighted sum of co-firing rates (Fig. 5B):

$$\dot{q}^{\Sigma\chi}[t_k] = \sum_{m=0}^{N-1} \dot{w}_m \dot{r}_m[t_k] \qquad \text{(Eq. 12)}$$

where $\dot{w}_n$ is a synaptic weight assigned to the nth co-firing rate. To derive the synaptic weights in Eq. 12, the pseudoinverse method was used to find a weight vector that minimized the error between $\dot{\mathbf{q}}$ and $\dot{\mathbf{q}}^{\Sigma\chi}$ for a training set of HD cell spike trains. Decoding accuracy was then tested on an independent test set of spike trains, derived from different behavior data. Fig. 5C shows $\dot{\mathbf{q}}$ and $\dot{\mathbf{q}}^{\Sigma\chi}$ for a 10s example simulation where $\tau_u = \tau_v = 200$ ms. Weight fitting was repeated at different time offsets between $\dot{\mathbf{q}}$ and $\dot{\mathbf{q}}^{\Sigma\chi}$ (since a time delay is introduced by the decay kernels in the

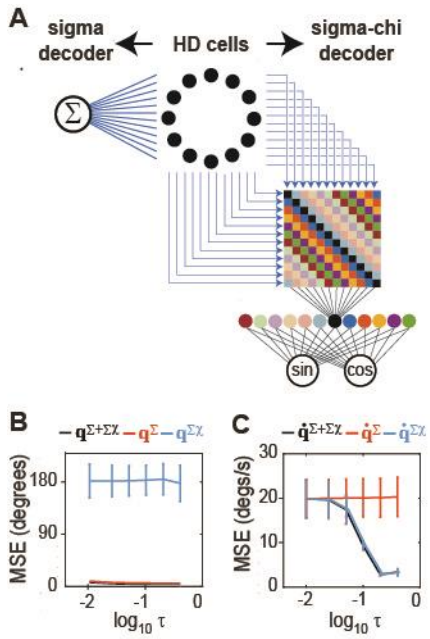

Figure 6. *Conjugate representations of position and velocity.* A) Spike trains from a ring of 12 HD cells are fed to a sigma or sigma-chi decoder. B) Decoding error (MSE, y-axis) was computed over a range of integration time constants: τ=.4, .2, .1, .05, .025, .01 s (x-axis, plotted on a $\log_{10}$ scale); head angle was accurately decoded from HD cell firing rates ($\mathbf{q}^{\Sigma}$) for all τ, but was near chance levels when decoded from co-firing rates ($\mathbf{q}^{\Sigma\chi}$), and decoding from both channels ($\mathbf{q}^{\Sigma+\Sigma\chi}$) did not improve upon decoding from firing rates alone. C) Angular velocity was accurately decoded from HD cell co-firing rates ($\dot{\mathbf{q}}^{\Sigma\chi}$) using sufficiently large integration time constant (τ>.1), but could not be decoded from firing rates ($\dot{\mathbf{q}}^{\Sigma}$) at any τ; decoding from both channels ($\dot{\mathbf{q}}^{\Sigma+\Sigma\chi}$) did not improve upon decoding from co-firing rates alone.

model), and the best fits were obtained when $\dot{\mathbf{q}}^{\Sigma\chi}$ was delayed from $\dot{\mathbf{q}}$ by approximately twice the value of the integration time constant used in the simulation (Fig. 2B). This is to be expected since $\dot{\mathbf{R}}$ is obtained from two sequential integration steps (using decay constants τ_u and τ_v), and illustrates the fact that sigma-chi units perform an operation of *neural differentiation* to derive $\dot{\mathbf{q}}$ from $\mathbf{q}$. This differentiation process may be regarded as an inversion of the standard *path integration* process by which HD cells are proposed to derive $\mathbf{q}$ from $\dot{\mathbf{q}}$ in attractor-integrator network models (Zhang, 1996). Since the velocity signal encoded by $\dot{\mathbf{R}}$ is delayed in time, it shall be referred to as a *post-positional* velocity signal, to distinguish it from *pre-positional* velocity signals (such as vestibular outputs) that normally would be used for angular path integration. A neural circuit that compares pre- versus post-positional velocity signals might provide a mechanism for setting the gain of path integration in an attractor-integrator network (see Discussion).

Conjugacy of firing rates and co-firing rates

We have seen that $\mathbf{q}$ can be recovered from HD cell firing rates using the sigma decoder (Figs. 1, 2A), and $\dot{\mathbf{q}}$ can be recovered from HD cell co-firing rates using the sigma-chi decoder (Figs. 2B, 5B). What happens if we swap the decoders, and thereby attempt to recover $\mathbf{q}$ from co-firing rates with the sigma-chi decoder, and recover $\dot{\mathbf{q}}$ from firing rates with the sigma decoder? We shall write $\mathbf{q}^{\Sigma\chi}$ to denote position recovered from co-firing rates by the sigma-chi decoder, and $\dot{\mathbf{q}}^{\Sigma}$ to denote velocity recovered from firing rates via the sigma decoder.

To derive $\mathbf{q}^{\Sigma\chi}$, HD cell co-firing rates $\dot{\mathbf{R}}$ (instead of firing rates) were delivered as input to the sine and cosine decoder neurons (Fig. 6A). The pseudoinverse method was then used to find a weight vector that minimized error between $\mathbf{q}^{\Sigma\chi}$ and $\mathbf{q}$. Decoding accuracy was tested on a novel set of spike trains derived from independent head angle data. Fig. 1E shows that $\mathbf{q}^{\Sigma\chi}$ (blue line) did not accurately estimate the true head angle for the 10 s example dataset. To further test whether co-firing rates contained information about $\mathbf{q}$, we used the pseudoinverse method to fit a weighted

sum of both $\mathbf{R}$ and $\dot{\mathbf{R}}$ to $\mathbf{q}$, thereby obtaining a prediction $\mathbf{q}^{\Sigma+\Sigma\chi}$ of the head angle which was derived simultaneously from both firing rates and co-firing rates. Over 10 independent simulations with different head angle data (Fig. 6B), we found that $\mathbf{q}^{\Sigma}$ accurately predicted $\mathbf{q}$ over a wide range of integration time constants, but $\mathbf{q}^{\Sigma\chi}$ could not accurately predict $\mathbf{q}$ at any value of the integration time constant, and $\mathbf{q}^{\Sigma+\Sigma\chi}$ was not a more accurate predictor of $\mathbf{q}$ than $\mathbf{q}^{\Sigma}$. Hence, decoding head angle from firing rates and co-firing rates together was not more accurate than decoding from firing rates alone. From this, we conclude that co-firing rates of simulated HD cell spike trains only conveyed information about $\dot{\mathbf{q}}$, but not $\mathbf{q}$.

To derive $\dot{\mathbf{q}}^{\Sigma}$, the HD cell firing rates $\mathbf{R}$ (instead of co-firing rates) were delivered as input to a sigma neuron (Fig. 6A), which computed their weighted sum (Eq. 7). The pseudoinverse method was then used to find a weight vector that minimized error between $\dot{\mathbf{q}}^{\Sigma}$ and $\dot{\mathbf{q}}$. Decoding accuracy was tested on a novel set of spike trains derived from independent head angle data. Fig. 5C shows that the angular velocity recovered from the sigma decoder, $\dot{\mathbf{q}}^{\Sigma}$ (red line), did not accurately estimate the true angular velocity for the 10 s example dataset. To further test whether firing rates contained information about $\dot{\mathbf{q}}$, we fit a weighted sum of both $\mathbf{R}$ and $\dot{\mathbf{R}}$ to $\dot{\mathbf{q}}$, thereby obtaining a prediction $\dot{\mathbf{q}}^{\Sigma+\Sigma\chi}$ of the angular velocity which was obtained simultaneously from both firing rates and co-firing rates. Over 10 independent simulations with different head angle data (Fig. 6C), we found that $\dot{\mathbf{q}}^{\Sigma\chi}$ accurately predicted $\dot{\mathbf{q}}$ for sufficiently large values of the integration time constant, $\dot{\mathbf{q}}^{\Sigma}$ could not accurately predict $\dot{\mathbf{q}}$ at any value of the integration time constant, and $\dot{\mathbf{q}}^{\Sigma+\Sigma\chi}$ was not a more accurate predictor of $\dot{\mathbf{q}}$ than $\dot{\mathbf{q}}^{\Sigma\chi}$. Hence, decoding angular velocity from firing rates and co-firing rates together was not more accurate than decoding from co-firing rates alone (Fig. 5C). From this, we conclude that co-firing rates of simulated HD cell spike trains only conveyed information about $\dot{\mathbf{q}}$, but not about $\mathbf{q}$.

These simulations show that when simulated HD cell spike trains encode only the head angle (but not angular velocity) in their firing rates, the firing rate and co-firing rate channels convey orthogonal representations of position and velocity. Firing rates exclusively encode information about angular position (and not angular velocity), whereas co-firing rates exclusively encode information about angular velocity (and not angular position).

Computing speed by differentiating grid cell spike trains

In much the same way that HD cells encode a periodic representation of an animal's angular head position, grid cells encode a periodic representation of an animal's translational position within a spatial environment. In this section, it is shown that when grid cell spike trains are fed as input to the sigma-chi decoder, sigma-chi neurons behave similarly to "speed cells" that have been reported in the hippocampus and entorhinal cortex (Kropf et al., 2015; Hinman et al., 2016; Gois & Tort, 2018). This provides yet another example of how sigma-chi neurons can perform neural differentiation, by deriving a speed signal from a position signal.

Simulation of grid cell spike trains

When a rat runs on a circular track, grid cells fire periodically as a function of the distance travelled around the track's circumference (Pierre-Yves et al., 2019). To simulate this periodic firing, grid cell spike trains were generated from position data that was obtained as a rat ran laps

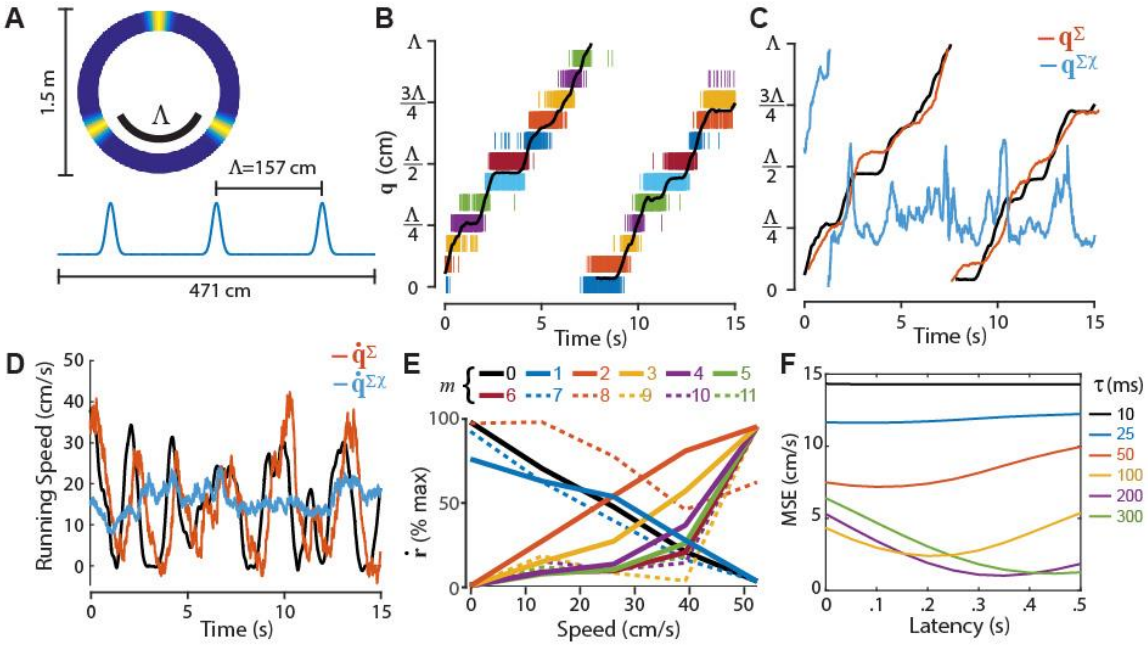

Figure 7. *Decoding position and running speed from grid cells.* A) Von Mises tuning functions were used to simulate periodic spatial tuning of grid cells on a circular track. B) Black line shows 15 s sample of position data, $\mathbf{q}$; rasters show spike trains of 12 grid cells. C) True position (black line) superimposed over position decoded from firing rates ($\mathbf{q}^{\Sigma}$) and co-firing rates ($\mathbf{q}^{\Sigma\chi}$). D) True running speed (black line) superimposed over running speed decoded from firing rates ($\dot{\mathbf{q}}^{\Sigma}$) and co-firing rates ($\dot{\mathbf{q}}^{\Sigma\chi}$). E) Speed tuning of co-firing rates generated by different sigma-chi neurons (indexed by m). F) Latency of speed tuning is proportional to the value of integration time constants.

on a 1.5 m diameter circular track while harnessed to a boom arm (Jayakumar et al., 2019). The rat's positon on the track was sampled at 1 KHz by the angle of the boom arm, yielding a time series of angles measured in radians, $\boldsymbol{\phi} = \{\phi_0, \phi_1, \cdots, \phi_k, \cdots, \phi_K\}$. For simplicity, the vertex spacing of simulated grid cells was assigned to be exactly one third of the distance around the track, $\Lambda = C/3$, where $C = 471$ cm is the track circumference. Each grid cell thus fired at three stable preferred locations during every lap around the track (Fig. 7A). Grid cell tuning curves were simulated using the same Von Mises distribution described above for simulating HD cell tuning curves (Eq. 3), except that $q_k = \phi_k/3$ now represents the rat's angular position within the grid spacing interval, Λ, rather than the head azimuth angle. For grid cell simulations, Von Mises tuning parameters were $R_{max} = 100$ Hz and $\kappa = 0.25$; the spatial phases of the grids, $\{\hat{q}_1, \hat{q}_2, \cdots, \hat{q}_N\}$, were evenly spaced over Λ. As described above for HD cell simulations, Eq. 3 was used to threshold a pseudorandom number generator and stochastically determine whether grid cell n fired a spike at time t_k. Binary values generated by this stochastic process filled a spike response matrix (Eq. 2), in which all spike trains exhibited Poisson rate statistics. In rodents, grid cell firing is typically modulated by theta rhythm, so grid cells do not generate Poisson spike trains. But here, we disregard theta modulation of grid cells.

Decoding position and speed from grid cell spike trains

Fig. 7B shows spike rasters for 12 simulated grid cells over a 15 s time period during which the rat ran almost 2/3 lap on the track (which is nearly 2 complete traversals of the spacing interval, Λ). Fig. 7C shows that the sigma decoder accurately recovers $\mathbf{q}$ (but fails to recover

running speed) from grid cell firing rates ($\tau_u = \tau_v = 200$ ms in these simulations). Conversely, Fig. 7D shows that the sigma-chi decoder accurately recovers running speed (but fails to recover $\mathbf{q}$) from grid cell co-firing rates. When grid cell spike trains are used as inputs to the sigma-chi decoder, the sigma-chi units exhibit tuning for running speed (Fig. 7E) that is qualitatively similar to the tuning of "speed cells" in the rodent entorhinal cortex and hippocampus (Kropf et al., 2015; Hinman et al., 2016; Gois & Tort, 2018). The speed signal encoded by co-firing rates is delayed in time by an amount proportional to the integration time constants τ_u and τ_v. Hence, the sigma-chi units are best tuned for the animal's past running speed (Fig. 7F), rather than present or future running speed. Consequently, sigma-chi units behave most similarly to a subset of speed cells in the rodent brain which have been observed to lag the animal's running speed in time (Kropf et al., 2015).

Computing positon by integrating theta cell spike trains

Simulations presented above show that if a population of spiking neurons (HD cells or grid cells) encodes a position signal in their firing rates, then they encode a velocity signal in their co-firing rates. Neural differentiation can thus be accomplished by sigma-chi neurons which convert the co-firing rate code for velocity into a firing rate code for velocity. Suppose now that we wish to invert this relationship, so that velocity is encoded by firing rates, and position is encoded by co-firing rates. Simulations presented below show that position information can be recovered from theta cell co-firing rates using a sigma-chi decoding process similar to that used above for recovering velocity information from HD cell or grid cell co-firing rates, and velocity information can be recovered from theta cell firing rates using the same sigma decoding process that was used above to recover position information from HD cell or grid cell firing rates.

Simulation of theta cell spike trains

To simulate phase coding of position by theta cells, we assume the existence of a *reference oscillator* against which theta cells shift their phases as a function of the animal's position. To mimic the rhythmicity of theta cell spike trains, all simulations used a reference oscillator with a constant frequency of 7 Hz (14π radians/sec). The time-varying phase of a theta cell can then be expressed as an offset from this reference oscillator,

$$\theta_n[t_k] = \psi_n[t_k] - \psi_0[t_k], \qquad \text{(Eq. 13)}$$

where ψ_0 is the reference phase and ψ_n is the phase of theta cell n. Here, all of the simulated theta cells shifted their phases against the reference oscillator (and none remained in fixed synchrony with it), so the reference oscillator was not explicitly represented by any of the theta cell spike trains. We may now define a *phase response matrix*,

$$\mathbf{\Theta} = \begin{bmatrix} \boldsymbol{\theta}_1 \\ \boldsymbol{\theta}_2 \\ \vdots \\ \boldsymbol{\theta}_N \end{bmatrix} = \{\Theta_0, \Theta_1, \dots, \Theta_k, \dots, \Theta_K\}, \qquad \text{(Eq. 14)}$$

where each column, $\Theta_k = \{\theta_1[t_k], \theta_2[t_k], \dots, \theta_N[t_k]\}^T$, gives the instantaneous phases for N theta cells at time t_k, and each row, $\boldsymbol{\theta}_n = \{\theta_n[t_0], \theta_n[t_1], \cdots, \theta_n[t_K]\}$, is a time series of phases for theta

cell n. Since θ_n is an angular variable, it can encode the animal's position on a spatially periodic interval. The animal's position within this interval shall be denoted q_n, defined as follows:

$$q_n[t_k] = 2\pi \frac{x[t_k]}{\lambda_n}, \qquad \text{(Eq. 15)}$$

where $x[t_k]$ is the total integrated distance that the animal has travelled around the track at time t_k, and λ_n is the distance over which θ_n shifts by one full theta cycle against the reference oscillator. The dependence of θ_n upon angular position may then be written

$$\theta_n[t_k] = \hat{\theta}_n + q_n[t_k], \qquad \text{(Eq. 16)}$$

where $\hat{\theta}_n$ is a phase offset parameter for theta cell n. Eq. 16 forces theta cells to behave as velocity controlled oscillators (VCOs) like those used in oscillatory interference models of spatial coding (Burgess et al., 2007). As in these prior models, the burst frequency, ω_n, of each theta cell varies as a function of the animal's running speed,

$$\omega_n[t_k] = \omega_0 + 2\pi \frac{v[t_k]}{\lambda_n}, \qquad \text{(Eq. 17)}$$

where $v[t_k]$ is the running speed at time t_k, and ω_0 is the frequency of the reference oscillator in radians/s. In simulations presented below, we shall permit λ_n to take either positive or negative values. If $\lambda_n > 0$, then ω_n increases with running speed, and θ_n precesses in phase against the reference oscillator. By contrast, if $\lambda_n < 0$, then ω_n decreases with running speed, and the reference oscillator precesses in phase against θ_n.

To compute the probability of spiking at each time step, we first created a "seed spike train" for each theta cell, denoted $\tilde{\mathbf{s}}_n$. This is a binary spike response function (Eq. 1) containing a single spike at every time step where theta cell n passes through perfect phase synchrony with the reference oscillator. The probability of spiking for theta cell n was then computed

$$p_n[t_k] = R_{max}(\tilde{\mathbf{s}}_n * \mathbf{g}), \qquad \text{(Eq. 18)}$$

where R_{max} is the maximum spike probability within a single time step, and $\mathbf{g}$ is a Gaussian kernel of unit amplitude. Here we used $\sigma = 25$ ms as the width of the Gaussian kernel in all simulations. To prevent the spike probability from exceeding R_{max} in any time bin, convolution was performed separately on even and odd numbered spikes within $\tilde{\mathbf{s}}_n$ (see Methods).

Ring oscillators

To construct a phase code for position, we shall group theta cells into subpopulations that form *ring oscillators* (Blair et al., 2014). Each ring oscillator is a circular array of theta cells through which a "bump" of activity circulates at a rate of once per theta cycle. To simulate bump circulation, phase offset parameters of theta cells within a ring are staggered at even spacings throughout the cycle by assigning $\hat{\theta}_p = 2\pi(p-1)/P$, where p indexes theta cells within the ring, and P is the total number of theta cells within a ring ($P = 12$ for all simulations presented here).

Our present objective shall be to construct a phase code that perfectly segregates information about position and velocity into the co-firing rate and firing rate channels, respectively. That is, the co-firing rate channel shall only convey information about position (but not velocity), and the firing rate channel shall only convey information about velocity (but not position). To

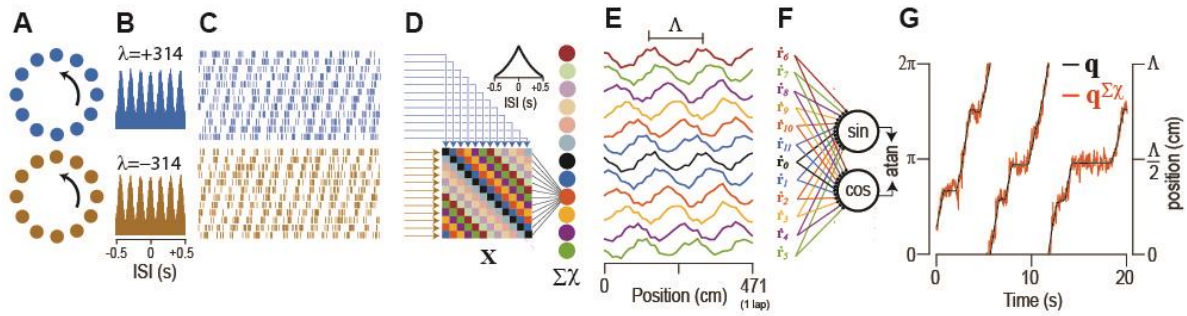

Figure 8. *Sigma-chi decoder recovers position from theta cell co-firing rates.* A) Two sets of 12 theta cells resided in ring oscillators with phase slopes of equal and opposite sign. B) Autocorrelgrams for theta cells in each ring. C) Rasters show 2 s sample of theta-modulated spike trains in the two rings. D) Sigma-chi decoder converts theta cell spike trains into chi rates (**X**) and then into co-firing rates encoded by activity of sigma-chi neurons (inset shows autocorrelogram for a sigma-chi neuron). E) Sigma-chi neurons behave like grid cells with periodic spatial tuning on the circular track. F) Sine and cosine components of angular position on the interval Λ are decoded via vector summation. G) The atan2 function converts output from sine and cosine decoder neurons into an accurate prediction, $\mathbf{q}^{\Sigma\chi}$, of position on the track.

achieve this perfect segregation, it is necessary to define pairs of ring oscillators, a and b, composed from theta cells with phase slopes of the same magnitude but opposing sign (Fig. 8A). Hence, if the phase slope for theta cells in ring a is denoted by λ_a, then the slope for cells in ring b must be $\lambda_b = -\lambda_a$. Assuming $\lambda_a > 0$, then theta cells in ring a precess (shift backward in phase) against the reference oscillator by one cycle per traversal of the distance λ_a, whereas cells in ring b process (shift forward in phase) against the reference oscillator by one cycle over the same distance. Fig. 8B shows example autocorrelograms for theta cells residing in a pair of ring oscillators with $\lambda_a = C/1.5 = 314$ cm and $\lambda_a = -C/1.5 = -314$ cm. Raster plots of spike trains for these theta cells are shown in Fig. 8C.

Decoding position from theta cell co-firing rates

Since theta cell phases are dependent upon q_n (Eq. 16), the angular position can be decoded from co-firing rates via the sigma-chi decoding process, which in this case has four steps: $\mathbf{S} \rightarrow \vec{\mathbf{X}} \rightarrow \dot{\mathbf{R}} \rightarrow \mathbf{Y} \rightarrow \mathbf{q}^{\Sigma\chi}$. In this section, we shall write $\mathbf{q}^{\Sigma\chi}$ to denote the time series of angular positions recovered from co-firing rates via the sigma-chi decoder, and $\mathbf{q}$ to denote the time series of true positions.

<u>Step 1: Deriving chi rates from spike trains</u>. The first decoding step, $\mathbf{S} \rightarrow \vec{\mathbf{X}}$, converts pairs of theta cell spike trains into chi rates, $\boldsymbol{\chi}_{i,j}$, using Eq. 9 above. To recover position information from $\boldsymbol{\chi}_{i,j}$, it is necessary for theta cells i and j to reside in different ring oscillators, so that the two cells will shift phase against one another as a function of the animal's position. Moreover, to obtain co-firing rates that exclusively encode position and not velocity (which is the goal of our current didactic exercise, but is by no means a requirement for neural coding of position and velocity in the brain), it is necessary for the rings containing cells i and j to have phase slopes of identical magnitude but opposing sign (that is, $\lambda_i = -\lambda_j$). A pair of theta cells meeting these requirements will shift through one cycle of phase against each other each time the animal traverses a distance equal to $\Lambda = |\lambda|/2$, where $|\lambda|$ is the shared magnitude of the phase slope for cells i and j. Fig. 8 shows an example with $|\lambda| = 314$ cm, so that $\Lambda = 157$ cm.

Step 2: Pooling chi rates to derive co-firing rates. The second decoding step, $\vec{\mathbf{X}} \rightarrow \dot{\mathbf{R}}$, pools chi rates from multiple theta cell pairs to derive a vector of co-firing rates. Given two ring oscillators that each contain P theta cells, there are P^2 unique ordered pairings between theta cells that reside in different rings, forming a $P \times P$ matrix of chi values (Fig. 8D). The rows and columns of this matrix can be sorted by the preferred phases, $\hat{\theta}_1, \hat{\theta}_2 \cdots, \hat{\theta}_P$, of theta cells in each ring. At each time step, t_k, we may define a 2D matrix, $\mathbf{X}_k$, in which each entry contains the instantaneous chi rate, $\chi_{i,j}[t_k]$, for theta cells i and j. This is the same matrix structure that was defined for pairs of HD cells in Fig. 4A above, except that here, the preferred firing phase of theta cells is substituted for the preferred head angle of HD cells. Hence, the main diagonal of $\mathbf{X}_k$ contains chi rates for pairs of theta cells that share the same phase offset parameter, $\hat{\theta}_n$, within their respective ring oscillators. Flanking the main diagonal, there are $N-1$ diagonal bands composed from entries containing chi rates for pairs of theta cells that share the same difference between their phase offset parameters, $\Delta\hat{\theta}_{i,j} = \hat{\theta}_j - \hat{\theta}_i$. As illustrated above (Fig. 4A), we may index these diagonal bands by $m = 0,1,2, \ldots, P-1$, such that the main diagonal ($i = j$) is indexed by $m = 0$, and each non-zero index m references a band containing chi rates between pairs of theta cells with preferred phases separated by a common offset, $\Delta\hat{\theta}_m = m \times 2\pi/P$. Activation of sigma-chi unit m can then be expressed as a co-firing rate, $\dot{r}_m$, obtained by summing all chi rates along a single band, as in Eq. 10 above. Since sigma-chi units pool inputs across all phases of theta, the time series $\dot{\mathbf{r}}_m$ is not itself modulated by theta (Fig. 8D, inset). Fig. 8E shows that each co-firing rate $\dot{\mathbf{r}}_m$ exhibits spatially periodic positional tuning, and therefore, each sigma-chi unit behaves like a grid cell with vertex spacing equal to Λ and spatial phase equal to $\Delta\hat{\theta}_m/2\pi$. It is thus possible to decode angular position, ϕ, from the vector of co-firing rates, in much the same way that position was decoded above from firing rates of simulated grid cell spike trains (Fig. 7C).

Step 3: Converting co-firing rates into angle components. The third decoding step, $\dot{\mathbf{R}} \rightarrow \mathbf{Y}$, converts co-firing rates into sine and cosine components of the animal's periodic angular position, ϕ, within the interval Λ. A pair of decoder neurons extracts the sine and cosine components of ϕ (Fig. 8F). The pseudoinverse method was used to assign weights minimizing the error for estimating $\sin(\phi)$ and $\cos(\phi)$.

Step 4: Converting angle components into periodic position. The fourth decoding step, $\mathbf{Y} \rightarrow \mathbf{q}^{\Sigma\chi}$, converts the sine and cosine components of ϕ into a prediction of the animal's position within the interval Λ. The atan2 function was used to obtain ϕ in radians from $\sin(\phi)$ and $\cos(\phi)$, and radians were then converted to distance by $q = \Lambda \times \phi/2\pi$ (Fig 8G).

Decoding velocity from theta cell firing rates

We now show that the animal's running speed can be decoded from theta cell firing rates via the sigma decoding process, which in this case has two steps: $\mathbf{S} \rightarrow \mathbf{R} \rightarrow \dot{\mathbf{q}}^{\Sigma}$. In this section, we shall write $\dot{\mathbf{q}}^{\Sigma}$ to denote the time series of running speeds recovered from the sigma decoder, and $\dot{\mathbf{q}}$ to denote the time series of true running speeds.

Step 1: Deriving theta cell firing rates from their spike trains. The first decoding step, $\mathbf{S} \rightarrow \mathbf{R}$, converts theta cell spike trains into firing rates. For simulations presented here, theta cell spike trains were converted into firing rates using Eq. 5. As explained above, each theta cell's burst frequency varies with running speed in accordance with Eq. 16. However, we define "firing rate" to mean the rate at which individual spikes occur—not the rate at which theta bursts occur—so it

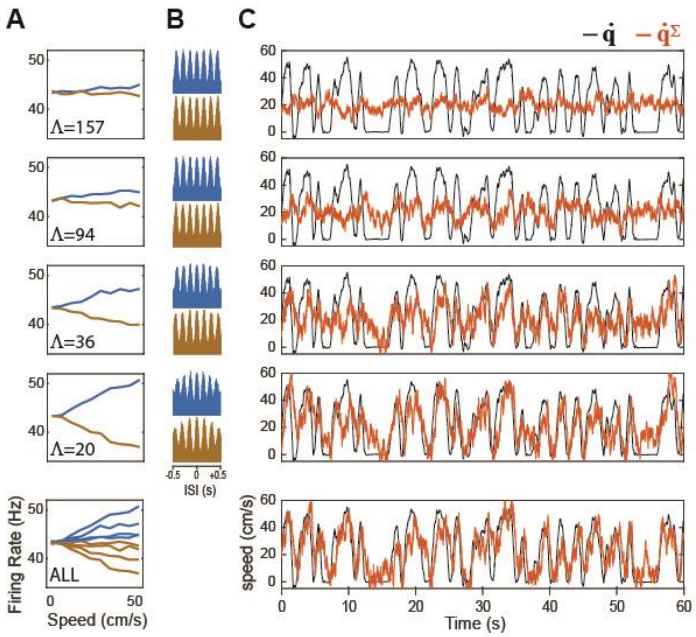

Figure 9. *Sigma decoder recovers velocity from theta cell firing rates.* A) Graphs plot dependence of theta cell firing rates (y-axis) upon running speed (x-axis) for different values of the phase slope parameter, Λ; theta cells with positive and negative phase slopes are plotted blue and brown, respectively. B) Autocorrelograms for theta cells plotted in 'A.' C) Actual running speed $\dot{\mathbf{q}}$ (black) superimposed with decoded speed $\dot{\mathbf{q}}^{\Sigma}$ (red) during a 60 s period of running on the circular track; top four graphs show $\dot{\mathbf{q}}^{\Sigma}$ decoded from 24 theta cells with phase slopes (12 positive, 12 negative) in 'A'; bottom graph shows running speed decoded from all theta cells in top folour graphs combined (96 theta cell in total, 48 with positive and 48 with negative phase slopes).

does not automatically follow from Eq. 17 that theta cell firing rates must vary with running speed. Nonetheless, since a theta cell's spike probability oscillates with its burst frequency (Eq. 18), it turns out that theta cells do indeed behave as "speed cells" with firing rates that are modulated by running speed. Firing rates of theta cells residing in paired rings a and b were modulated by running speed with a steepness that was inversely proportional to their phase slopes, λ_a and λ_b (Fig. 9A). Theta cells with positive phase slopes ($\lambda_a > 0$) increased their firing rates with running speed, and those with negative phase slopes ($\lambda_b < 0$) decreased their firing rates with running speed. Fig. 9B shows autocorrelograms for simulated theta cells over a range of different phase slopes.

<u>Step 2: Decoding running speed from firing rates</u>. The second decoding step, $\mathbf{R} \rightarrow \dot{\mathbf{q}}^{\Sigma}$, converts theta cell firing rates into an estimate of the animal's running speed. We have already seen that theta cell firing rates are modulated by running speed, so in principle, it should be easy to decode the animal's running speed from theta cell firing rates. However, when we used the pseudoinverse method to derive weights that minimized the error between $\dot{\mathbf{q}}^{\Sigma}$ and $\dot{\mathbf{q}}$ for theta cells with $|\lambda| = 314$ cm, the fit was not good when the decoder was tested on data independent from the training set (Fig 9C, top panel). This is because the accuracy of speed decoding is proportional to the slope with which velocity modulates theta cell firing rates, which in turn is inversely proportional to $|\lambda|$, and setting $|\lambda| = 314$ cm yields a slope that is too shallow for accurate speed decoding. This problem is easily remedied by using theta cells with steeper phase slopes, which increases the slope of velocity modulation (and also decreases the vertex spacing, Λ, of grid cells formed via the sigma-chi decoding process; see Fig. 10A). Fig. 9C shows that velocity decoding progressively improved with steeper slopes of velocity modulation, becoming quite accurate for $|\lambda| = 41$ cm, which yields a vertex spacing of $\Lambda = 20.5$ cm for grid cells simulated by sigma-chi neurons; this is within the range of experimentally observed vertex spacings for grid cells (Hafting et al., 2005).

There is no biological requirement for all ring oscillators to share the same value of $|\lambda|$, so we simulated multiple ring oscillators with different phase slopes. Four pairs of ring oscillators (8 rings in all, with 12 theta cells in each ring) containing a total of 96 theta cells were assigned phase

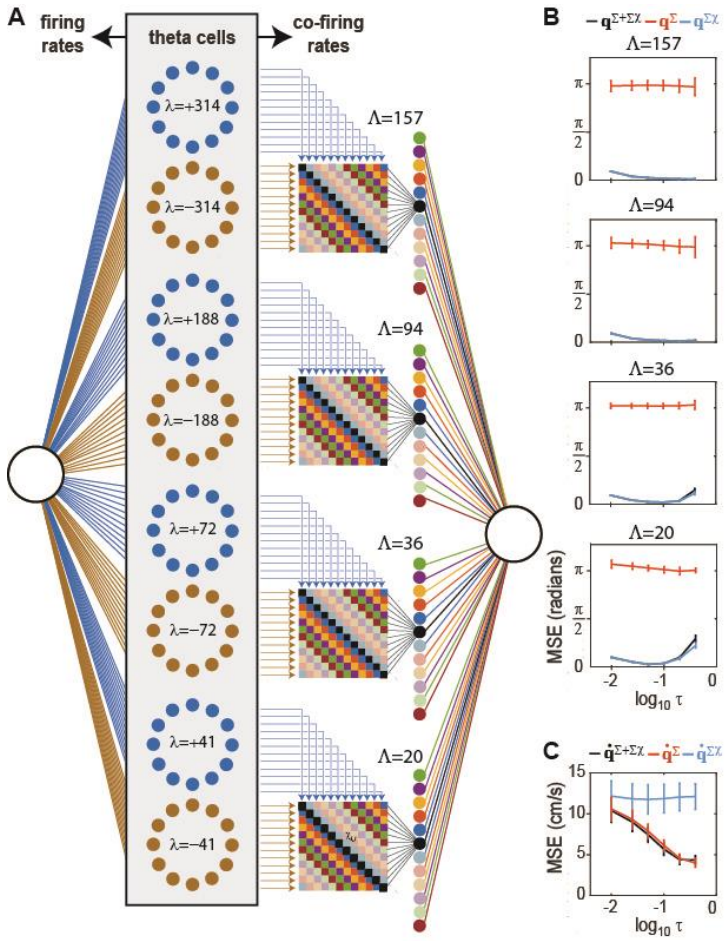

Figure 10. *Segregation of position and velocity into co-firing and firing rate channels.* A) Four complementary pairs of ring oscillators contain a total of 96 theta cells; firing rates are fed to a sigma decoder, and co-firing rates are fed to a sigma-chi decoder. B) Angular position ($\mathbf{q}$, y-axis) is accurately decoded from co-firing rates ($\mathbf{q}^{\Sigma\chi}$) but not firing rates ($\mathbf{q}^{\Sigma}$) of theta cells for all spatial periods (Λ) and integration time constants (τ=.4, .2, .1, .05, .025, or .01 s; x-axis plots τ on a log scale). C) Running speed ($\dot{\mathbf{q}}$, y-axis) is accurately decoded from firing rates ($\dot{\mathbf{q}}^{\Sigma}$) but not co-firing rates ($\dot{\mathbf{q}}^{\Sigma\chi}$) of theta cells for sufficiently large integration time constants (x-axis).

slopes $\lambda_1 = \pm 314$ cm, $\lambda_2 = \pm 188$ cm, $\lambda_3 = \pm 72$ cm, and $\lambda_4 = \pm 41$ cm. Fig. 10B shows that when spike trains from these four ring pairs were fed into a sigma-chi decoder (configured so that chi rates were derived within but not between ring pairs), it was possible to accurately recover the animal's position $\mathbf{q}$ on intervals of length $\Lambda_1 = 157$ cm, $\Lambda_2 = 94$ cm, $\Lambda_3 = 36$ cm, and $\Lambda_4 = 20.5$ cm, which are the vertex spacings of grid cells simulated by sigma-chi neurons formed from each ring pair. A sigma neuron summing inputs from all 96 theta cells (using weights assigned via the pseudoinverse method on an independent training dataset) accurately recovered the animal's running speed from theta cell firing rates (Fig. 10C).

Conjugate coding of position and velocity

Results shown in Figs. 8-10 demonstrate that theta cells can simultaneously encode position information in their co-firing rates, while encoding velocity (running speed) information in their firing rates. As explained above, the theta cell population was constructed to contain pairs of ring oscillators with equal and opposite phase slopes (Fig. 9A), so that $\mathbf{q}$ was decoded from each ring pair on a spatially periodic interval of length Λ (which was determined by the phase slopes for that ring pair). We now show that if co-firing rates are computed exclusively within (and not between) these complementary ring pairs, then position ($\mathbf{q}$) and running speed ($\dot{\mathbf{q}}$) information become perfectly segregated into the co-firing and firing rate channels, respectively. This can be

demonstrated by swapping the decoders, and thereby attempting to recover $\dot{\mathbf{q}}$ from co-firing rates and $\mathbf{q}$ from firing rates. We shall write $\mathbf{q}^{\Sigma}$ to denote position recovered from firing rates, and $\grave{\mathbf{q}}^{\Sigma\chi}$ to denote velocity recovered from co-firing rates.

To derive $\dot{\mathbf{q}}^{\Sigma\chi}$, a weighted sum of theta cell co-firing rates $\{\dot{\mathbf{r}}_1, \dot{\mathbf{r}}_2, \ldots, \dot{\mathbf{r}}_N\}^T$ was computed, retaining the constraint that co-firing rates were only computed within (and not between) complementary ring pairs. The pseudoinverse method was then used to find a weight vector that minimized error between $\dot{\mathbf{q}}^{\Sigma\chi}$ and $\dot{\mathbf{q}}$. Decoding accuracy was tested on a novel set of spike trains derived from independent behavior data. Fig. 10C shows that $\dot{\mathbf{q}}^{\Sigma\chi}$ did not accurately estimate the true running speed. To further test whether co-firing rates contained information about $\dot{\mathbf{q}}$, we attempted to recover running speed from a weighted sum of both firing rates and co-firing rates, $\dot{\mathbf{q}}^{\Sigma+\Sigma\chi}$, and used the pseudoinverse method to minimize error between $\dot{\mathbf{q}}^{\Sigma+\Sigma\chi}$ and $\dot{\mathbf{q}}$. Over 10 independent simulations with different behavior data, we found that decoding $\dot{\mathbf{q}}$ from theta cell firing rates and co-firing rates together was not more accurate than decoding from firing rates alone (Fig. 10C). That is, the accuracy of $\dot{\mathbf{q}}^{\Sigma+\Sigma\chi}$ was not better than the accuracy of $\dot{\mathbf{q}}^{\Sigma}$. From this, we conclude that firing rates of simulated theta cells only conveyed information about $\dot{\mathbf{q}}$, and not about $\mathbf{q}$.

To derive $\mathbf{q}^{\Sigma}$, a weighted sum of theta cell firing rates $\{\mathbf{r}_1, \mathbf{r}_2, \ldots, \mathbf{r}_N\}^T$ was computed, and the pseudoinverse method was used to find a weight vector that minimized error between $\mathbf{q}^{\Sigma}$ and $\mathbf{q}$. Decoding accuracy was then tested on a novel set of spike trains derived from independent behavior data. Fig. 5B shows that $\mathbf{q}^{\Sigma}$ did not accurately estimate the animal's true position on the interval Λ. To further test whether firing rates contained information about $\mathbf{q}$, we attempted to recover running speed from a weighted sum of both firing rates and co-firing rates, $\mathbf{q}^{\Sigma+\Sigma\chi}$, and used the pseudoinverse method to minimize error between $\mathbf{q}^{\Sigma+\Sigma\chi}$ and $\mathbf{q}$. Over 10 independent simulations with different behavior data, we found that decoding $\mathbf{q}$ from theta cell firing rates and co-firing rates together was no more accurate than decoding from co-firing rates alone (Fig. 10B). From this, we conclude that if co-firing rates are computed from complementary pairs of theta ring oscillators, then they only convey information about $\mathbf{q}$, and not about $\dot{\mathbf{q}}$.

Computing co-firing rates from non-complementary ring oscillator pairs

Given a set of N ring oscillators, there are $(N^2 - N)/2$ unique non-ordered pairings between different rings. In the simulations of Fig. 10, we used 8 ring oscillators (4 pairs of complementary rings), which yields a total of 28 non-ordered pairings. However, we only computed co-firing rates from 4 of these 28 possible pairings, because as explained above, the 4 pairings between complementary rings have the special property of yielding co-firing rates which only contain position (and not velocity) information.

It is certainly possible to derive co-firing rates from non-complementary ring pairs, but co-firing rates computed in this way will contain information about both position and velocity, rather than just position. To demonstrate this, Fig. 11 shows results from simulations of 4 ring oscillators—each containing 12 theta cells (for a total of 48 theta cells in all)—which were all assigned to have positive phase slopes: $\lambda_1 = +314$ cm, $\lambda_2 = +188$ cm, $\lambda_3 = +55$ cm, and $\lambda_4 = +39$ cm. There are 6 unique non-ordered pairings among these 4 rings, and since all rings have

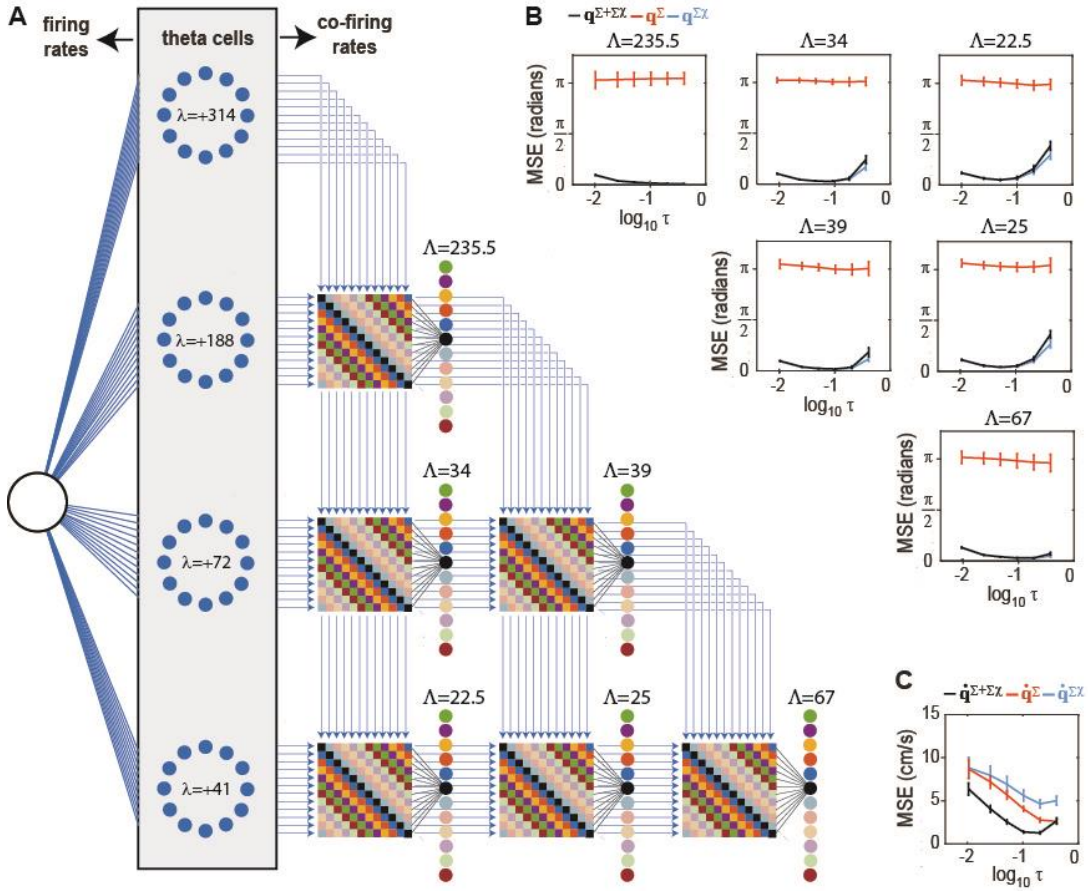

Figure 11. *Position and velocity coding with non-complementary ring oscillators.* A) Co-firing rates are derived from six unique pairings among four ring oscillators, all with positive phase slopes. B) Angular position can be decoded from co-firng rates on six different length intervals (Λ=22.5, 25, 34, 39, 67, 235.5 cm); decoding error (MSE, y-axis) is low when angular position is decoded from theta cell co-firing rates ($\mathbf{q}^{\Sigma\chi}$) but near chance levels when decoded from firing rates ($\mathbf{q}^{\Sigma}$); x-axis plots integration time constant (τ=.4, .2, .1, .05, .025, .01 s) on $\log_{10}$ scale. C) Runnin speed ($\mathbf{q}$, y-axis) can be decoded from either firing rates ($\mathbf{q}^{\Sigma}$) or co-firing rates ($\mathbf{q}^{\Sigma\chi}$) of theta cells, and is most accurate when decoded from both together ($\mathbf{q}^{\Sigma+\Sigma\chi}$).

positive phase slopes, there are no complementary pairs. Fig. 11B shows that position can only be decoded from firing rates (but not co-firing rates) of theta cells residing in non-complementary ring pairs, a result similar to that shown above for complementary ring pairs. However, running speed can be recovered from either firing rates or co-firing rates of theta cells residing in non-complementary ring pairs, and the most accurate decoding is obtained when running speed is recovered from both together (Fig. 11C).

DISCUSSION

Here we have shown that populations of spiking neurons can embed two orthogonal codes within their spike trains: a *firing rate code* derived from the spikes of individual neurons, and a *co-firing rate code* derived from correlations among spike trains of different neurons. Two biologically inspired decoding methods—*sigma* and *sigma-chi* decoding—were used to demonstrate that these two codes behave as *conjugates* of one another: if one code conveys information about position,

then the other conveys information about velocity. This conjugate relationship makes it very natural for a population of N periodically tuned neurons to encode the position and velocity of a freely moving animal by implementing a mapping of the form $(q, \dot{q}) \longrightarrow (R, \dot{R})$, where the domain $(q, \dot{q})$ is a phase space with orthogonal axes for the animal's position (q) and velocity $(\dot{q})$, and the range $(R, \dot{R})$ is a neural coding space composed from orthogonal axes for the firing rates (R) and co-firing rates $(\dot{R})$ of a set of spike trains. Hence, a single set of spike trains can simultaneously encode information about an animal's position and velocity in its firing rates and co-firing rates. This conjugate coding principle may be important for understanding functional connections between neural populations in the hippocampal system.

Biological substrates for decoding firing and co-firing rates

A wide range of theoretical models have been proposed to explain how neural populations in the hippocampal system—such as place cells, grid cells, border cells HD cells, speed cells, and theta cells—might be functionally interconnected with one another to solve navigational problems such as cognitive mapping, self-localization, and trajectory planning (for review, see Hinman et al, 2018). Most of these models have been simulated using networks of simplified linear neurons that compute weighted sums of their firing rate inputs, and thus derive their outputs as a function of R, but not of $\dot{R}$, similar to the sigma decoder in our simulations. By contrast, biological neurons have large dendritic trees with detailed branching patterns, endowing them with complex anatomical and electrotonic structure. Such neurons can support nonlinear computations—including detection of correlations among spike trains—that are not reducible to simple weighted linear summation of firing rate inputs (for review, see Mel, 2007). Hence, biological neurons may be able to derive their outputs not only from R, but also from $\dot{R}$, similar to the sigma-chi decoder in our simulations. Supporting this possibility, it has been shown that the dendrites of hippocampal pyramidal cells (Makara & Magee, 2013) and entorhinal stellate cells (Schmidt-Hieber et al., 2017) can perform nonlinear integration of their inputs in ways that should allow them to derive their outputs from correlations among their input spike trains. And spatial information can be decoded not only from the firing rates of hippocampal neurons, but also form correlations among their spike trains. For example, a rodent's head direction can be more accurately reconstructed using information from firing rates and spike correlations combined than from either source alone (Peyrache et al., 2015). In addition, decoding a rodent's position from the spike rates and spike phases of hippocampal place cells is more accurate than decoding from rate or phase alone (Jensen and Lisman, 2000). Some theta-modulated neurons in the lateral septum appear to encode spatial information almost exclusively in their spike phases, and barely at all in their firing rates (Tingley & Buzsaki, 2018).

In a biologically realistic network where neural units extract information from spike correlations as well as from firing rates, the conjugate coding principle may become relevant (and possibly essential) for understanding how information about position and velocity are exchanged between different neural subpopulations in the hippocampal system. It may thus not be possible for models constructed from simple linear integrator units to generate accurate or complete predictions about functional interconnections between neural populations in the hippocampal system. To illustrate this, let us review how several key predictions of prior models might need to be modified to account for the possibility of conjugate coding in biological networks.

Integrating velocity to compute position

Spatially tuned neurons are thought to compute an animal's position in two ways: by measuring the animal's displacement from fixed landmarks in the surrounding environment, and by measuring the animal's current position relative to its prior position (McNaughton et al., 1996). The latter process requires integrating the animal's movement velocity over time to compute its position, a procedure known as *path integration.* Three types of models have been proposed to explain how hippocampal networks might perform path integration: *attractor networks*, *reservoir computing networks*, and *oscillatory interference models*.

Attractor networks

Attractor networks have been used to simulate path integration by HD cells (Zhang, 1996; Song & Wang, 2005), place cells (Samsonovich and McNaughton, 1997; Conklin & Eliasmith, 2005; Hedrick & Zhang, 2016), and grid cells (Fuhs & Touretzky, 2006; Guanella and Kiper, 2007; Burak & Fiete, 2009). Although these models differ in their implementation details, they all share two core features of attractor networks in common (see Knierim & Zhang, 2012). First, a population of neurons with position-tuned firing rates (such as HD, place, or grid cells) are reciprocally interconnected with one another via lateral inhibition, causing a localized "activity bump" to form as a stable attractor state of the network. Second, the symmetry of lateral connections among position-tuned neurons is controlled by neurons with velocity-tuned firing rates, which can push the activity bump through the network along trajectories that mirror the animal's trajectory through space. Analysis of spike trains from pairs of simultaneously recorded HD cells (Peyrache et al., 2015; Butler & Taube, 2017) and grid cells (Yoon et al., 2013) has revealed evidence for attractor dynamics in these networks, and experimentalists have reported connections in the entorhinal grid cell network that resemble connectivity patterns predicted by standard attractor network models (Couey et al., 2013; Fuchs et al., 2016).

However, the attractor network models cited above were all simulated using linear neurons (either non-spiking units or LIF units) that derived their outputs exclusively from R, and not from $\dot{R}$. Connectivity patterns predicted by these models are thus founded upon an unrealistic assumption: that neural units derive their outputs exclusively from the firing rates of their inputs. This assumption is almost certainly false, as evidenced by the fact that dendrites of hippocampal pyramidal cells and entorhinal stellate cells can perform nonlinear integration of their inputs, and could thus derive their outputs from correlations among their input spike trains (Makara & Magee, 2013; Schmidt-Hieber et al., 2017). The conjugate coding principle we have described here implies that neural representations of position and velocity—and thus connections among neurons that encode these variables—could look very different in a network composed from such nonlinear neurons (as opposed to the simplified linear neurons used in attractor models).

In a standard attractor network composed from linear units, velocity signals that push the activity bump are extracted from the firing rates of velocity-tuned neurons; these models thus predict feedforward connections from velocity-tuned neurons to position-tuned neurons. But in a biological attractor network, velocity signals could instead be extracted from the co-firing rates of position-tuned neurons (as in Figs. 4 & 7), so the feedforward velocity inputs predicted by standard attractor networks might not exist at all. Instead, they could be replaced (or augmented) by functionally equivalent connections from one population of position tuned neurons to another (e.g., from entorhinal grid cells to hippocampal place cells, or vice versa). It should be noted that velocity signals encoded by co-firing rates tend to be delayed in time by an amount proportional the time constant of integration (see Fig. 2), which could introduce a time lag into the path integrated

position signal when velocity is extracted from co-firing rates. However, position signals encoded by the firing rates HD cells and grid cells are often seen to prospectively lead the animal's true position (Muller & Kubie, 1989; Blair & Sharp, 1995; Mehta et al., 1997; Almeida et al., 2012), which would help to compensate for any time lag if velocity signals were derived from the co-firing rates of these neurons. Standard attractor networks also predict lateral inputs to position tuned neurons from neighboring position tuned neurons, but under conjugate coding, these connections too could be replaced or augmented by functionally equivalent alternatives, such as inputs to position tuned neurons (e.g., place cells or grid cells) from velocity-tuned neurons (e.g., theta cells) that encode position in their co-firing rates rather than their firing rates.

In summary, the conjugate coding principle suggests that biological and artificial attractor networks may be subject to radically different constraints upon their connectivity, and therefore, artificial attractor network models composed from linear neurons may be quite limited in their ability generate accurate predictions about connectivity in biological networks.

Reservoir computing networks

Reservoir computing models of path integration are recurrent neural networks trained from example data (via gradient descent methods) to convert time-varying velocity signals into time-varying position signals (Abbott et al., 2016, DeNeve & Machens, 2016). It has recently been shown that neurons with periodic spatial tuning—similar to entorhinal grid cells—can emerge spontaneously in a recurrent network trained to perform spatial path integration (Banino et al., 2018). Most reservoir computing models of path integration use recurrent networks composed from linear neurons, so the inputs and outputs to these networks encode velocity and position signals as vectors of neural firing rates (not spike train correlations). However, unlike attractor models, recurrent connections within a reservoir computing network are sculpted by learning, and it is thus possible that when a recurrent network of spiking neurons is trained to perform path integration, error-driven learning could cause the formation of neural microcircuits that extract information about position or velocity from correlations among spike trains, and not just firing rates. Hence, learning might allow a reservoir computing network composed from linear neurons to extract information from spike correlations at the circuit level, rather than the level of individual neurons. Perhaps if a recurrent network were constructed from the "ground up" using spiking neurons that perform nonlinear integration of their inputs—similar to the sigma-chi neurons in our simulations—then fewer neurons would be needed to achieve criterion path integration performance in a reservoir computing model (because individual nonlinear neurons would be capable of performing computations on spike correlations that would otherwise require circuit-level interactions among linear neurons). Training a recurrent network of sigma-chi neurons to perform path integration would require differentiating Eq. 9 to derive a cost function that supports convergent learning. If this could be achieved, then it would be intriguing to investigate whether conjugate coding principles naturally emerge when a recurrent network of sigma-chi neurons is trained to perform path integration. Phenomena such as oscillatory rhythms that support co-firing rate codes might emerge spontaneously from the training of such a network, in a manner similar to the way that grid cells emerge spontaneously when a network of linear neurons is trained to perform path integration (Banino et al., 2018). The emergent firing properties and connectivity patterns in a trained network of recurrently connected sigma-chi neurons might bear closer resemblance to biology than those that emerge from networks of linear neurons.

Oscillatory interference models

Oscillatory interference models are explicitly designed to encode position information using correlated neural activity, rather than firing rates. These models propose that the brain contains *velocity-controlled oscillators* (VCOs) that shift phase against one another at a rate that depends upon the animal's movement velocity (Burgess et al., 2007; Geisler et al., 2007). Consequently, the phase offsets between the oscillators depend upon the animal's positon in space. Assuming that VCO oscillations are represented by the spike trains of neurons that burst rhythmically at the theta frequency, then the VCOs map the animal's position into a representational space where each dimension measures time intervals (normalized by the theta cycle period) between pairs of spikes that are fired by *different* neurons (that is, cells synchronized to different VCOs). This is in marked contrast with attractor and reservoir computing models, which map the animal's position into a representational space where each dimension measures time intervals between pairs of spikes that are fired by the *same* neuron (that is, firing rates).

Early oscillatory interference models demonstrated how individual grid cells (Burgess et al., 2007; Giocomo et al., 2007a,b) or place cells (Blair et al., 2008) could derive their position-tuned firing rates by detecting of location-specific synchrony among inputs from theta VCOs. This mechanism can account not only for the spatial firing properties of place and grid cells, but also for temporal firing properties such as theta rhythmicity, phase precession (O'Keefe & Recce, 1993; Hafting et al., 2008), and modulation of theta oscillations by running speed (Geisler et al., 2007; Welday et al., 2011; Jeewajee et al., 2014). Some of these early oscillatory interference models (Burgess et al., 2007; Giocomo et al., 2007a,b) simulated nonlinear multiplicative interactions among VCO inputs to grid cells, while others were based upon linear summation of VCO inputs (Welday et al., 2011). However, these early models were focused upon mimicking the firing properties of individual grid or place cells, rather than modeling path integration or other network-level computations. Later models proposed novel "hybrid" architectures for performing path integration through a combination of both attractor dynamics and oscillatory interference (Bush & Burgess, 2014; Hasselmo & Shay, 2014). Despite incorporating oscillatory interference mechanisms rooted in spike correlations, these models were simulated by networks of linear neurons that derived their outputs by computing weighted sums of their inputs, and then converted these weighted sums into spike trains using LIF or Izhikevic spike dynamics. The connectivity patterns predicted by these models might be different—and perhaps more biologically accurate—if they were reformulated using model neurons that perform nonlinear integration of their inputs.

Differentiating position to compute velocity

The hippocampal system contains neural populations that encode velocity as well as position. Angular velocity cells have been reported in the head direction system (Sharp, 1996; Stackman & Taube, 1998), and "speed cells" have been reported in the hippocampus and entorhinal cortex (Kropf et al., 2015; Hinman et al., 2016; Gois & Tort, 2018). Some of these velocity signals may originate in other brains regions, such as vestibular circuits that detect inertial velocity, or motor circuits that generate self-movement. Simulations presented above show how velocity signals might also be computed by differentiating position signals encoded by spatially tuned neurons within the hippocampal system itself (Figs. 4 & 7).

Cellular versus circuit mechanisms for neural differentiation

Circuit-level mechanisms for neural differentiation have been proposed previously, for example by classical models of visual motion sensitivity (Hubel & Weisel, 1962). In the visual system, some neurons are tuned for the direction in which a visual stimulus moves through the visual field, and this kind of directional tuning can be modeled by neural circuits that integrate inputs from position-tuned neurons with receptive fields that are arranged sequentially along the preferred path of motion (Baccus et al., 2008). Such models bear a strong resemblance to our simulations of angular velocity cells (Fig. 4C) and speed cells (Fig. 7E), in which sigma-chi neurons derived velocity signals from position signals. But in these classical models of visual motion detection, directional tuning is typically derived from circuit-level mechanisms (such as asymmetric lateral inhibition), whereas in our simulations, velocity tuning was instead achieved by the non-commutative chi operation (Eq. 9), which might be performed at the cellular level (rather than the circuit level) by biological neurons. Calcium imaging experiments have revealed that in visual cortex, most neurons that receive input from orientation-tuned cells pool their inputs across the entire 360° range of edge orientations, and exhibit "hot spots" for specific orientations in different parts of their dendritic tree (Jia et al., 2010). This arrangement is similar to what would be expected if visual cortex neurons were computing co-firing rates by pooling their inputs across multiple orientation phases, in a manner similar to the way that sigma-chi neurons pooled inputs across multiple phases of head angle (Fig. 4) or theta phase (Fig. 10) in our simulations.

Pre- versus post-positional velocity signals

We use the term "post-positional" velocity signal to describe speed or velocity signals that are derived by differentiating position signals. This is to draw a distinction with "pre-positional" velocity signals that are derived from the motor or vestibular systems, independently of any positional code. There is evidence that pre- and post-positional velocity signals may both co-exist in the hippocampal system: some speed cells are prospectively correlated with the animal's future running speed, while others are retrospectively correlated with the past running speed (Kropf et al., 2015). It would be expected that post-positional speed cells should lose their speed modulation following any disruption of the position signal that they differentiate to derive their speed tuning. For example, if post-positional speed cells derive their tuning by differentiating inputs from grid cells, then disrupting grid cells should also disrupt speed cells. Medial septum inactivation has been shown to impair grid cell firing (Brandon et al., 2011; Koenig et al. 2011) but not speed cell firing (Hinman et al., 2016) in entorhinal cortex; however, entorhinal speed cells are biased toward prospective coding (Kropf et al., 2015), and may thus be predominated by pre-positional rather than post-positional speed cells. Hippocampal speed cells tend to be biased toward retrospective speed coding (Kropf et al., 2015), so if these speed cells differentiate position signals, they might be more likely to lose their speed tuning (or shift to prospective speed coding) after place or grid cells are inactivated. To our knowledge, this has not yet been experimentally tested.

Some neural computations in the hippocampal system might depend upon both pre- and post-positional velocity signals. For example, it has recently been shown from place cell recordings that the gain of the hippocampal path integration can be modified by prolonged exposure to a cue conflict between inertial and non-inertial self-motion cues (Jayakumar et al., 2019). Presumably, such cue conflict generates error signals that recalibrate the gain of the path integrator, and one way to compute such error signals would be to calculate the difference between pre- versus post-positional velocity signals. Hence, differentiation of position signals to compute post-positional velocity signals might be essential for calibrating the gain of path integration in the hippocampal system, and conjugate coding may play a significant role in this process.

Velocity coding in multiple dimensions

In open-field environments, place cells and grid cells exhibit robust spatial tuning in two dimensions. To support position tuning in two dimensions, a path integrator would require inputs from a two-dimensional velocity signal, which encodes both the speed and direction of the animal's movements. To our knowledge, a firing rate code for two-dimensional velocity has not convincingly been observed in the rodent hippocampal system. Speed cells may contribute to encoding the non-directional component of velocity in two dimensions, but a firing rate code for allocentric movement direction has not been reported. The entorhinal cortex does contain neurons that are tuned for head direction (Giocomo et al., 2014), and many grid cells are selective not only for the animal's position but also for the direction in which its head is facing (Sargolini et al., 2006; Wills et al., 2012). However, these entorhinal populations are tuned for head azimuth angle rather than for allocentric movement direction, and two dimensional path integration using a head direction signal is not as accurate as integration of a true two-dimensional movement signal (Roudies et al., 2015).

The conjugate coding principle suggests that a firing rate code for allocentric movement velocity would not need to exist, because a population of neurons that encodes a two-dimensional position signal in its firing rates (such as place or grid cells) would be expected to encode a two-dimensional velocity in its co-firing rates. Hence, the co-firing rates of grid cells (rather than the firing rates of speed or head direction cells) may serve as the primary substrate for encoding velocity signals that support two-dimensional path integration.

An uncertainty principle for neural coding

The above simulations of position and velocity coding invite a comparison with the *uncertainty principle* from physics, which states that the more we know about a particle's position, the less we know about its momentum (or velocity), and vice versa. In physics, this trade-off is formalized by the inequality $\sigma_x \sigma_p \geq \hbar/2$ (where $\hbar$ is the reduced Planck constant), which places a lower bound on the product of standard deviations for the probability distributions of position, ,σ_x, and momentum, σ_p (Kennard, 1927). We postulate that an analogous uncertainty principle may hold for the accuracy with which position and velocity (or more generally, any stimulus variable and its time derivative) can be decoded from neural data. If $\mathbf{S}$ is a set of spike trains generated by a population of neurons, and V is a vector space (such as the space of firing rates or co-firing rates) into which $\mathbf{S}$ can be mapped, then we may write q_V and $\dot{q}_V$ to denote unbiased estimates for a stimulus, q, and its time derivative, $\dot{q} = dq/dt$, that are decoded from V. We postulate that the product of the variances obeys $\operatorname{var} q_V \operatorname{var} \dot{q}_V \geq C,$ where $\operatorname{var} q_V$ and $\operatorname{var} \dot{q}_V$ denote the variances of the decoding errors, and C denotes a Cramer-Rao lower bound for the product of the decoding variances. We further hypothesize that if R denotes a vector space of firing rates onto which $\mathbf{S}$ can be mapped, and $\dot{R}$ denotes an orthogonal space of co-firing rates onto which $\mathbf{S}$ can also be mapped, then the more accurately q is encoded by R, the less accurately it can be encoded by $\dot{R}$, and vice versa. To state this more formally, let q_R and $\dot{q}_R$ denote unbiased estimates for q and $\dot{q}$ decoded from R, and let $q_{\dot{R}}$ and $\dot{q}_{\dot{R}}$ be unbiased estimates of q and $\dot{q}$ decoded from $\dot{R}$. It is postulated that the variances of these estimates for q obey two relations: 1) $\operatorname{var} q_R \operatorname{var} q_{\dot{R}} \geq C_q,$ where C_q is a lower bound on the variance for decoding q from $R \times \dot{R}$, and 2) $\operatorname{var} \dot{q}_R \operatorname{var} \dot{q}_{\dot{R}} \geq C_{\dot{q}},$ where $C_{\dot{q}}$ is a lower bound on the variance for decoding $\dot{q}$ from $R \times \dot{R}$. Further theoretical

analyses are necessary to demonstrate whether these relations hold true, and if so, under what specific conditions.

Summary and Conclusions

Neuroscience researchers are sometimes prone to "ratism"—a bias to regard the firing rates of spiking neurons as the primary coordinate basis of the neural code. Under the influence of this bias, it is reflexively assumed that if individual neurons are tuned for some particular variable (such as head angle, spatial position, or running speed), then a population of such neurons exists mainly to encode distributed representations of that same variable using vectors of neural firing rates. While it is certainly true that information can be encoded by (and decoded from) population vectors of neural firing rates, it is does not follow from this that the space of firing rate vectors is the only representational space into which information is mapped by neural spike trains. It is necessary to recognize and appreciate that the same population of neurons can encode different information when viewed through the "lenses" of different decoders.

Here, we have shown that there is a conjugate relationship between firing rate codes and spike correlation codes, which mirrors the uncertainty principle from physics. A firing rate code for position ($q \longrightarrow R$) can co-exist with a co-firing rate code for velocity ($\dot{q} \longrightarrow \dot{R}$), or a co-firing rate code for position ($q \longrightarrow \dot{R}$) can co-exist with a firing rate code for velocity ($\dot{q} \longrightarrow R$). More generally, a firing rate code for any time-varying stimulus can co-exist with a co-firing rate code for the time derivative of that stimulus, and vice versa. Hence, the conjugate coding principle described here may be useful for understanding neural coding not only in the hippocampal system, but in other brain systems as well. For example, the visual system encodes information about the position and as well as the velocity of objects in the visual field. Motor and proprioceptive systems processes information about the position and velocity of moving limbs. And neural circuits for reinforcement learning encode information about expected value and prediction error, which bear a relationship to one another that is similar to the relationship between position and velocity (prediction error is the time derivative of expected value, and expected value is the time integral prediction error). In all of these systems, the conjugate coding principle may be at work to embed orthogonal representations of stimuli and their time derivatives within the firing rates and co-firing rates of neural spike trains. Further theoretical and empirical analysis may help to elucidate how biological neurons extract information (at the level of single cells) from both firing rates and co-firing rates to efficiently perform useful computations.

Acknowledgements

We thank Manu Madhav and Ravi Jayakumar for position tracking data from the circular track, and Rose DeGuzman for assistance in collecting the head direction data from the open field. We also thank Kechen Zhang and Joseph Monaco for helpful feedback and discussion. This work was supported by a UCLA Cota-Robles Graduate Fellowship awarded to Ryan Grgrich.

METHODS

All simulations were carried out using MATLAB (source code available upon request).

Position Tracking

Simulated HD, grid, and theta cells were generated from position tracking data. Head direction data from the open field was obtained while a rat foraged freely for food pellets in a circular arena (diameter = 80 cm). Rats wore a pair of red and green light-emitting diodes (LEDs) spaced 11.25 cm apart from one another, and an overhead video camera sampled LED positions at *R*=30 Hz with a resolution of *P*=4.7 pixels/cm. Each LED's position was smoothed using a boxcar window 15 samples (0.5 s) wide, and the rat's head direction at each time step was estimated as $\arctan(\Delta y_i/\Delta x_i)$, where Δx_i and Δy_i denote the difference between the x and y coordinates of the red and green LEDs, respectively a the ith position sample. Position data from the circular track was obtained while rats ran laps on a 1.5 m diameter circular track enclosed within a planetarium-style dome, where an array of three visual landmarks was projected onto the interior surface to create an augmented reality environment (Jayakumar et al., 2019). The rat was attached to a boom arm that rotated around a joint in the center of the track, and the rat's position on the track was sampled at 100 Hz from an optical encoder of the boom angle in the center joint.

Generation of simulated spike trains

To simulate spike trains of HD cells or grid cells, we computed the probability of spiking at each time step using Eq. 3. The computed probability was then used as a threshold for a random number generator that output a real value between 0 and 1; a spike was placed in a given time step if the random value fell below the calculated probability threshold, yielding a binary spike response function (Eq. 1). For simulations of theta cell spike trains, the spike response function was generated in two steps. First we first created a "seed spike train" for each theta cell, containing a single spike at every time step where the theta cell's phase (computed using Eq. 16) passed through perfect phase synchrony with the reference oscillator. The probability of spiking for theta cell n was then computed by convolving the seed spike train with a Gaussian kernel (Eq. 18). A problem with this methods was that when seed spikes were spaced closer together than the width of the Gaussian kernel, it was possible for the convolution procedure to yield inappropriately large spike probabilities. To prevent this, the convolution was performed separately on even and odd numbered spikes within the seed spike train, so that no two spikes would be closer together than the width of the Gaussian kernel. The two convolution results were then merged by taking the maximum probability from either of the two results at each time step. The probabilities in the merged time series were then used as the probability threshold on the random number generator for outputting the theta cell's spike response function.

REFERENCES

Abbott, L. F., DePasquale, B., & Memmesheimer, R.-M. (2016). Building functional networks of spiking model neurons. *Nature Neuroscience*, *19*(3), 350. http://doi.org/10.1038/nn.4241

Baccus, S. A., Ölveczky, B. P., Manu, M., & Meister, M. (2008). A retinal circuit that computes object motion. *Journal of Neuroscience*, *28*(27), 6807–6817. http://doi.org/10.1523/JNEUROSCI.4206-07.2008

Banino, A., Barry, C., Uria, B., Blundell, C., Lillicrap, T., Mirowski, P., et al. (2018). Vector-based navigation using grid-like representations in artificial agents. *Nature*, *521*, 436. http://doi.org/10.1038/s41586-018-0102-6

Blair, H. T., & Sharp, P. E. (1995). Anticipatory head direction signals in anterior thalamus: evidence for a thalamocortical circuit that integrates angular head motion to compute head direction. *Journal of Neuroscience*, *15*(9), 6260–6270. http://doi.org/10.1523/JNEUROSCI.15-09-06260.1995

Blair, H. T., & Sharp, P. E. (1996). Visual and vestibular influences on head-direction cells in the anterior thalamus of the rat. *Behavioral Neuroscience*, *110*(4), 643–660. http://doi.org/10.1037/0735-7044.110.4.643

Blair, H. T., Gupta, K., & Zhang, K. (2008). Conversion of a phase- to a rate-coded position signal by a three-stage model of theta cells, grid cells, and place cells. *Hippocampus*, *18*(12), 1239–1255. http://doi.org/10.1002/hipo.20509

Blair, H. T., Wu, A., & Cong, J. (2014). Oscillatory neurocomputing with ring attractors: a network architecture for mapping locations in space onto patterns of neural synchrony. *Philosophical Transactions of the Royal Society B: Biological Sciences*. http://doi.org/10.1098/rstb.2012.0526

Brandon, M. P., Bogaard, A. R., Libby, C. P., Connerney, M. A., Gupta, K., & Hasselmo, M. E. (2011). Reduction of Theta Rhythm Dissociates Grid Cell Spatial Periodicity from Directional Tuning. *Science*, *332*(6029), 595–599. http://doi.org/10.1126/science.1201652

Burak, Y., & Fiete, I. R. (2009). Accurate Path Integration in Continuous Attractor Network Models of Grid Cells. *PLoS Computational Biology*, *5*(2), e1000291. http://doi.org/10.1371/journal.pcbi.1000291

Burgess, N., Barry, C., & O'Keefe, J. (2007). An oscillatory interference model of grid cell firing. *Hippocampus*, *17*(9), 801–812. http://doi.org/10.1002/hipo.20327

Bush, D., & Burgess, N. (2014). A Hybrid Oscillatory Interference/Continuous Attractor Network Model of Grid Cell Firing. *Journal of Neuroscience*, *34*(14), 5065–5079. http://doi.org/10.1523/JNEUROSCI.4017-13.2014

Butler, W. N., & Taube, J. S. (2017). Oscillatory synchrony between head direction cells recorded bilaterally in the anterodorsal thalamic nuclei. *Journal of Neurophysiology*. http://doi.org/10.1152/jn.00881.2016

Climer, J. R., Newman, E. L., & Hasselmo, M. E. (2013). Phase coding by grid cells in unconstrained environments: two-dimensional phase precession. *European Journal of Neuroscience*, *38*(4), 2526–2541. http://doi.org/10.1111/ejn.12256

Couey, J. J., Witoelar, A., Zhang, S.-J., Zheng, K., Ye, J., Dunn, B., et al. (2013). Recurrent inhibitory circuitry as a mechanism for grid formation. *Nature Neuroscience*, *16*(3), 318–324. http://doi.org/10.1038/nn.3310

De Almeida, L., Idiart, M., Villavicencio, A., & Lisman, J. (2012). Alternating predictive and short-term memory modes of entorhinal grid cells. *Hippocampus*, *22*(8), 1647–1651. http://doi.org/10.1002/hipo.22030

Denève, S., & Machens, C. K. (2016). Efficient codes and balanced networks. *Nature Neuroscience*, *19*(3), 375–382. http://doi.org/10.1038/nn.4243

Eliasmith, C. (2005). A Unified Approach to Building and Controlling Spiking Attractor Networks. *Neural Computation*, *17*(6), 1276–1314. http://doi.org/10.1162/0899766053630332

Fuchs, E. C., Neitz, A., Pinna, R., Melzer, S., Caputi, A., & Monyer, H. (2016). Local and Distant Input Controlling Excitation in Layer II of the Medial Entorhinal Cortex. *Neuron*, *89*(1), 194–208. http://doi.org/10.1016/j.neuron.2015.11.029

Fuhs, M. C., & Touretzky, D. S. (2006). A Spin Glass Model of Path Integration in Rat Medial Entorhinal Cortex. *Journal of Neuroscience*, *26*(16), 4266–4276. http://doi.org/10.1523/JNEUROSCI.4353-05.2006

Geisler, C., Robbe, D., Zugaro, M., Sirota, A., & Buzsáki, G. (2007). Hippocampal place cell assemblies are speed-controlled oscillators. *Proceedings of the National Academy of Sciences*, *104*(19), 8149–8154. http://doi.org/10.1073/pnas.0610121104

Giocomo, L. M., Stensola, T., Bonnevie, T., Van Cauter, T., Moser, M.-B., & Moser, E. I. (2014). Topography of Head Direction Cells in Medial Entorhinal Cortex. *Current Biology*, *24*(3), 252–262. http://doi.org/10.1016/j.cub.2013.12.002

Giocomo, L. M., Zilli, E. A., Fransén, E., & Hasselmo, M. E. (2007). Temporal Frequency of Subthreshold Oscillations Scales with Entorhinal Grid Cell Field Spacing. *Science*, *315*(5819), 1719–1722. http://doi.org/10.1126/science.1139207

Góis, Z. H. T. D., & Tort, A. B. L. (2018). Characterizing Speed Cells in the Rat Hippocampus. *Cell Reports*, *25*(7), 1872–1884.e4. http://doi.org/10.1016/j.celrep.2018.10.054

GUANELLA, A., KIPER, D., & VERSCHURE, P. (2011). A MODEL OF GRID CELLS BASED ON A TWISTED TORUS TOPOLOGY. *International Journal of Neural Systems*, *17*(04), 231–240. http://doi.org/10.1142/S0129065707001093

Hafting, T., Fyhn, M., Bonnevie, T., Moser, M.-B., & Moser, E. I. (2008). Hippocampus-independent phase precession in entorhinal grid cells. *Nature*, *453*(7199), 1248–1252. http://doi.org/10.1038/nature06957

Hafting, T., Fyhn, M., Molden, S., Moser, M.-B., & Moser, E. I. (2005). Microstructure of a spatial map in the entorhinal cortex. *Nature*, *436*(7052), 801–806. http://doi.org/10.1038/nature03721

Hasselmo, M. E., & Shay, C. F. (2014). Grid cell firing patterns may arise from feedback interaction between intrinsic rebound spiking and transverse traveling waves with multiple heading angles. *Frontiers in Systems Neuroscience*, *8*. http://doi.org/10.3389/fnsys.2014.00201

Hasselmo, M. E., Giocomo, L. M., & Zilli, E. A. (2007). Grid cell firing may arise from interference of theta frequency membrane potential oscillations in single neurons. *Hippocampus*, *17*(12), 1252–1271. http://doi.org/10.1002/hipo.20374

Hedrick, K. R., & Zhang, K. (2016). Megamap: flexible representation of a large space embedded with nonspatial information by a hippocampal attractor network. *Journal of Neurophysiology*. http://doi.org/10.1152/jn.00856.2015

Hinman, J. R., Brandon, M. P., Climer, J. R., Chapman, G. W., & Hasselmo, M. E. (2016). Multiple Running Speed Signals in Medial Entorhinal Cortex. *Neuron*, *91*(3), 666–679. http://doi.org/10.1016/j.neuron.2016.06.027

Hinman, J. R., Dannenberg, H., Alexander, A. S., & Hasselmo, M. E. (2018). Neural mechanisms of navigation involving interactions of cortical and subcortical structures. *Journal of Neurophysiology*. http://doi.org/10.1152/jn.00498.2017

HUBEL, D. H., & WIESEL, T. N. (1962). Receptive fields, binocular interaction and functional architecture in the cat's visual cortex. *The Journal of Physiology*, *160*(1), 106–154. http://doi.org/10.1113/jphysiol.1962.sp006837

Jacob, P.-Y., Capitano, F., Poucet, B., Save, E., & Sargolini, F. (2019). Path integration maintains spatial periodicity of grid cell firing in a 1D circular track. *Nature Communications*, *10*(1), 840. http://doi.org/10.1038/s41467-019-08795-w

Jayakumar, R. P., Madhav, M. S., Savelli, F., Blair, H. T., Cowan, N. J., & Knierim, J. J. (2019). Recalibration of path integration in hippocampal place cells. *Nature*, *566*(7745), 533. http://doi.org/10.1038/s41586-019-0939-3

Jeewajee, A., Barry, C., Douchamps, V., Manson, D., Lever, C., & Burgess, N. (2014). Theta phase precession of grid and place cell firing in open environments. *Philosophical Transactions of the Royal Society B: Biological Sciences*. http://doi.org/10.1098/rstb.2012.0532

Jensen, O., & Lisman, J. E. (2000). Position Reconstruction From an Ensemble of Hippocampal Place Cells: Contribution of Theta Phase Coding. *Journal of Neurophysiology*. http://doi.org/10.1152/jn.2000.83.5.2602

Jia, H., Rochefort, N. L., Chen, X., & Konnerth, A. (2010). Dendritic organization of sensory input to cortical neurons in vivo. *Nature*, *464*(7293), 1307. http://doi.org/10.1038/nature08947

Knierim, J. J., & Zhang, K. (2012). Attractor Dynamics of Spatially Correlated Neural Activity in the Limbic System. *Dx.Doi.org*. http://doi.org/10.1146/annurev-neuro-062111-150351

Koenig, J., Linder, A. N., Leutgeb, J. K., & Leutgeb, S. (2011). The Spatial Periodicity of Grid Cells is Not Sustained During Reduced Theta Oscillations. *Science*, *332*(6029), 592–595. http://doi.org/10.1126/science.1202333

Kropff, E., Carmichael, J. E., Moser, M.-B., & Moser, E. I. (2015). Speed cells in the medial entorhinal cortex. *Nature*, *523*(7561), 419–424. http://doi.org/10.1038/nature14622

Lever, C., Burton, S., Jeewajee, A., O'Keefe, J., & Burgess, N. (2009). Boundary Vector Cells in the Subiculum of the Hippocampal Formation. *Journal of Neuroscience*, *29*(31), 9771–9777. http://doi.org/10.1523/JNEUROSCI.1319-09.2009

Makara, J. K., & Magee, J. C. (2013). Variable Dendritic Integration in Hippocampal CA3 Pyramidal Neurons. *Neuron*, *80*(6), 1438–1450. http://doi.org/10.1016/j.neuron.2013.10.033

McNaughton, B. L., Barnes, C. A., Gerrard, J. L., Gothard, K., Jung, M. W., Knierim, J. J., et al. (1996). Deciphering the hippocampal polyglot: the hippocampus as a path integration system. *Journal of Experimental Biology*, *199*(1), 173–185.

Mehta, M. R., Barnes, C. A., & McNaughton, B. L. (1997). Experience-dependent, asymmetric expansion of hippocampal place fields. *Proceedings of the National Academy of Sciences*, *94*(16), 8918–8921. http://doi.org/10.1073/pnas.94.16.8918

Mel, B. W. (2007). Why have dendrites? A computational perspective. In G. Stuart (Ed.), *Dendrites* (2nd ed., pp. 421–440). Oxford University Press. doi:10.1093/acprof:oso/9780198566564.003.0016.

Muller, R. U., & Kubie, J. L. (1989). The firing of hippocampal place cells predicts the future position of freely moving rats. *Journal of Neuroscience*, *9*(12), 4101–4110. http://doi.org/10.1523/JNEUROSCI.09-12-04101.1989

O'Keefe, J., & Dostrovsky, J. (1971). The hippocampus as a spatial map. Preliminary evidence from unit activity in the freely-moving rat. *Brain Research*, *34*(1), 171–175. http://doi.org/10.1016/0006-8993(71)90358-1

O'Keefe, J., & Recce, M. L. (1993). Phase relationship between hippocampal place units and the EEG theta rhythm. *Hippocampus*, *3*(3), 317–330. http://doi.org/10.1002/hipo.450030307

Peyrache, A., Lacroix, M. M., Petersen, P. C., & Buzsáki, G. (2015). Internally organized mechanisms of the head direction sense. *Nature Neuroscience*, *18*(4), 569. http://doi.org/10.1038/nn.3968

Raudies, F., Brandon, M. P., Chapman, G. W., & Hasselmo, M. E. (2015). Head direction is coded more strongly than movement direction in a population of entorhinal neurons. *Brain Research*, *1621*, 355–367. http://doi.org/10.1016/j.brainres.2014.10.053

Samsonovich, A., & McNaughton, B. L. (1997). Path Integration and Cognitive Mapping in a Continuous Attractor Neural Network Model. *Journal of Neuroscience*, *17*(15), 5900–5920. http://doi.org/10.1523/JNEUROSCI.17-15-05900.1997

Sargolini, F., Fyhn, M., Hafting, T., McNaughton, B. L., Witter, M. P., Moser, M.-B., & Moser, E. I. (2006). Conjunctive Representation of Position, Direction, and Velocity in Entorhinal Cortex. *Science*, *312*(5774), 758–762. http://doi.org/10.1126/science.1125572

Savelli, F., Yoganarasimha, D., & Knierim, J. J. (2008). Influence of boundary removal on the spatial representations of the medial entorhinal cortex. *Hippocampus*, *18*(12), 1270–1282. http://doi.org/10.1002/hipo.20511

Schmidt-Hieber, C., Toleikyte, G., Aitchison, L., Roth, A., Clark, B. A., Branco, T., & Häusser, M. (2017). Active dendritic integration as a mechanism for robust and precise grid cell firing. *Nature Neuroscience*, *20*(8), 1114–1121. http://doi.org/10.1038/nn.4582

Sharp, P. (1996). Multiple Spatial/Behavioral Correlates for Cells in the Rat Postsubiculum: Multiple Regression Analysis and Comparison to Other Hippocampal Areas. *Cerebral Cortex*, *6*(2), 238–259. http://doi.org/10.1093/cercor/6.2.238","keywords":["hippocampus“,”fire

Skaggs, W. E., McNaughton, B. L., Wilson, M. A., & Barnes, C. A. (1996). Theta phase precession in hippocampal neuronal populations and the compression of temporal sequences. *Hippocampus*, *6*(2), 149–172. http://doi.org/10.1002/(SICI)1098-1063(1996)6:2<149::AID-HIPO6>3.0.CO;2-K

Solstad, T., Boccara, C. N., Kropff, E., Moser, M.-B., & Moser, E. I. (2008). Representation of Geometric Borders in the Entorhinal Cortex. *Science*, *322*(5909), 1865–1868. http://doi.org/10.1126/science.1166466

Song, P., & Wang, X.-J. (2005). Angular Path Integration by Moving “Hill of Activity”: A Spiking Neuron Model without Recurrent Excitation of the Head-Direction System. *Journal of Neuroscience*, *25*(4), 1002–1014. http://doi.org/10.1523/JNEUROSCI.4172-04.2005

Stackman, R. W., & Taube, J. S. (1998). Firing Properties of Rat Lateral Mammillary Single Units: Head Direction, Head Pitch, and Angular Head Velocity. *Journal of Neuroscience*, *18*(21), 9020–9037. http://doi.org/10.1523/JNEUROSCI.18-21-09020.1998

Taube, J. S., Muller, R. U., & Ranck, J. B. (1990). Head-direction cells recorded from the postsubiculum in freely moving rats. I. Description and quantitative analysis. *Journal of Neuroscience*, *10*(2), 420–435. http://doi.org/10.1523/JNEUROSCI.10-02-00420.1990

Tingley, D., & Buzsáki, G. (2018). Transformation of a Spatial Map across the Hippocampal-Lateral Septal Circuit. *Neuron*, *98*(6), 1229–1242.e5. http://doi.org/10.1016/j.neuron.2018.04.028

Welday, A. C., Shlifer, I. G., Bloom, M. L., Zhang, K., & Blair, H. T. (2011). Cosine Directional Tuning of Theta Cell Burst Frequencies: Evidence for Spatial Coding by Oscillatory Interference. *Journal of Neuroscience*, *31*(45), 16157–16176. http://doi.org/10.1523/JNEUROSCI.0712-11.2011

Wills, T., Barry, C., & Cacucci, F. (2012). The abrupt development of adult-like grid cell firing in the medial entorhinal cortex. *Frontiers in Neural Circuits*, *6*. http://doi.org/10.3389/fncir.2012.00021

Wilson, M. A., & McNaughton, B. L. (1993). Dynamics of the hippocampal ensemble code for space. *Science*, *261*(5124), 1055–1058.

Yoder, R. M., & Taube, J. S. (2014). The vestibular contribution to the head direction signal and navigation. *Frontiers in Integrative Neuroscience*, *8*, 32. http://doi.org/10.3389/fnint.2014.00032

Yoon, K., Buice, M. A., Barry, C., Hayman, R., Burgess, N., & Fiete, I. R. (2013). Specific evidence of low-dimensional continuous attractor dynamics in grid cells. *Nature Neuroscience*, *16*(8), 1077–1084. http://doi.org/10.1038/nn.3450

Zhang, K. (1996). Representation of spatial orientation by the intrinsic dynamics of the head-direction cell ensemble: a theory. *Journal of Neuroscience*, *16*(6), 2112–2126. http://doi.org/10.1523/JNEUROSCI.16-06-02112.1996